

Cite this: DOI: 00.0000/xxxxxxxxxx

Mapping the Configuration Space of Half-Heusler Compounds via Subspace Identification for Thermoelectric Materials Discovery [†]

Angela Pak,^a Kamil Ciesielski,^b Maria Wroblewska^b, Eric S. Toberer^b, and Elif Ertekin^aReceived Date
Accepted Date

DOI: 00.0000/xxxxxxxxxx

Half-Heuslers are a promising family for thermoelectric (TE) applications, yet only a small fraction of their potential chemistries has been experimentally explored. In this work, we introduce a distinct computational high-throughput screening approach designed to identify underexplored yet promising material subspaces, and apply it to half-Heusler thermoelectrics. We analyze 1,126 half-Heuslers satisfying the “18 valence electron rule,” including 332 predicted to be semiconductors, using electronic structure calculations, semi-empirical transport models, and thermoelectric quality factor β . Unlike conventional filtering workflows, our approach employs statistical analysis of candidate material groups to uncover trends in their collective behavior, providing robust insights and minimizing reliance on uncertain predictions for individual compounds. Our findings link *n*-type performance to ultra-high mobility at conduction band edges and *p*-type performance to high band degeneracy. Statistical correlations reveal elemental subspaces associated with high β . We identify two primary (Y- and Zr-containing) and two secondary (Au- and Ir-containing) subspaces that reinforce key physical design principles, making them promising candidates for further exploration. These recommendations align with previous experimental results on yttrium pnictides. Inspired by these insights, we synthesize and characterize rare-earth gold stannides (REAuSn), finding $\text{Sc}_{0.5}\text{Lu}_{0.5}\text{AuSn}$ to exhibit low thermal conductivity ($0.9\text{--}2.3\text{ Wm}^{-1}\text{K}^{-1}$ at 650 K). This work demonstrates alternative strategies for high throughput screening when using approximate but unbiased models, and offers predictive tools and design strategies for optimizing half-Heusler chemistries for TE performance.

1 Introduction

Half-Heuslers are a family of face-centered-cubic crystals with chemical formula ABC where A and B are transition metals and C is a p-block element. These elements crystallize in space group $F\bar{4}3m$, where the more electronegative of the two transition metals, B, occupies the FCC sublattice and A and C species form a rock salt structure.¹ The 18 valence electron half-Heuslers are particularly of interest in semiconductor applications due to their anticipated band gaps and stability,^{2,3} but only 188 of these chemistries have been realized experimentally as listed in the Inorganic Crystal Structure Database.⁴ Such realized compounds have shown promise for applications such as topological insulators and thermoelectrics (TEs).^{5–10} Yet, the 188 experimentally realized half-Heuslers represent only a small subset of all possible 18 valence

electron chemistries. Thus, the half-Heusler space offers a vast range of unique intermetallic chemistries and transport properties that have yet to be characterized. To fill this gap, we introduce a modified high-throughput materials screening workflow that is designed to identify subspaces, or families of related compounds, that are promising search spaces for new thermoelectrics.

The disparate properties required for good performance, as described by TE figure of merit zT , make TEs a challenging case for computational materials discovery. Figure of merit zT is a composite parameter that involves both intrinsic (e.g., intrinsic mobility and thermal conductivity^{11,12} and extrinsic (e.g., temperature and carrier concentration^{13,14}) properties. Prediction of intrinsic properties relies on models for electron and phonon transport and scattering.¹⁵ The need to evaluate transport coefficients, and other relevant material properties has motivated the design of “funnel” workflows, where candidate materials are passed through computational filters one by one.^{16–19}

Computational approaches to predicting transport properties, however, inherently involve trade-offs between accuracy and cost, ranging from semi-empirical transport descriptions,²⁰ to constant

^a University of Illinois at Urbana-Champaign, Urbana, IL 61801, USA; E-mail: ertekin@illinois.edu

^b Colorado School of Mines, Golden, CO 80401, USA.

[†] Electronic Supplementary Information (ESI) available: See DOI: 00.0000/00000000.

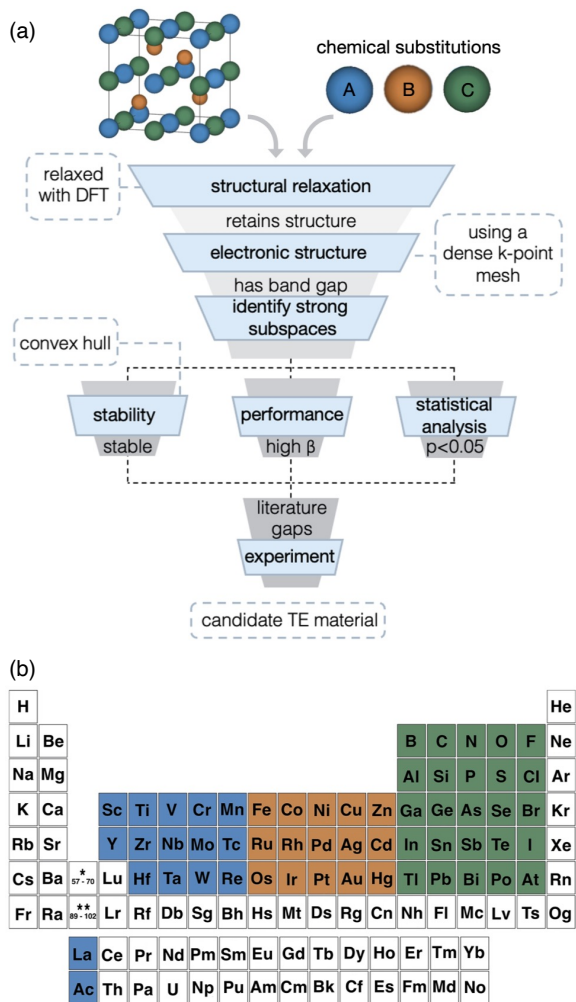


Fig. 1 Overview of the approach for identifying promising elemental subspaces in Half-Heusler thermoelectric materials. (a) The method resembles a funnel approach, but integrates parallel assessments of stability, performance, and statistical significance to identify optimal subspaces. (b) Elements evaluated for potential chemical substitution.

relaxation time Boltzmann transport equations,²¹ to fully first-principles mode-resolved calculations of scattering rates²². While fully first-principles approaches show the highest predictive capacity, they are not amenable to screening large material sets. Semi-empirical models, by contrast, are most suited for evaluating large numbers of materials and have been successfully applied to TE materials discovery,^{12,14,23} but their simplified and approximate nature limit quantitative precision.

These trade-offs present challenges for high-throughput screening workflows that rely on traditional “funnel” approaches. In standard funnel workflows, a large pool of candidate materials is gradually narrowed through a sequence of computational filters by passing only candidates that meet predefined criteria to the next stage. Materials that make it through the entire funnel are recommended for synthesis and experimental validation. While this approach can be effective, it has notable pitfalls. Early stage reliance on computationally inexpensive but approximate filters introduces uncertainty that propagates through later stages. Fur-

thermore, these workflows often rely on rank-ordered lists of performance descriptors^{14,17,24–28}, placing a heavy emphasis on the accuracy of individual predictions, over identifying broader patterns or trends in the material space. Approximate but unbiased models are prone to variability and noise, making individual property predictions less reliable. Trends, when analyzed collectively, serve as more reliable indicators of performance. Thus, strict rank-ordering risks overlooking candidates with valuable traits visible only when viewed across the broader material space.

To address these challenges, we present an alternative high-throughput screening approach centered on identifying promising subspaces within a broad materials space. We employ the dimensionless TE quality factor, β ,²⁰ alongside evaluations of electronic structure, thermodynamic stability, and transport properties to target key subspaces within the half-Heusler family (Figure 1a). Instead of sequential filtering, our method applies statistical analysis across the dataset to reveal robust, chemistry-based patterns, leveraging the collective behavior of groups over less reliable individual predictions. Unlike standard workflows, this methodology actively promotes integration of physical insights with computational screening, considering material stability, novelty, and future synthesis compatibility. Our approach focuses on element-based regions of half-Heusler chemical space where high TE performance aligns with stable chemistries, providing actionable insights for experimental synthesis. This intersection of performance and stability is visually represented in Figure 2. Such element-based subspaces provide advantages in their practicality, particularly for strategies like alloying to enhance properties.^{29–34}

Specifically, we analyze an extensive set of 1,126 candidate half-Heuslers with the chemical formula ABC, satisfying the 18-valence electron rule. These candidates were generated by selecting elements from the periodic table (Figure 1b), of which 332 are predicted to be semiconductors. To date, the vast majority of half-Heusler workflows start from considering only known chemistries or those that exist in online databases⁸, or limit the search to a narrow set of elements⁵, and often downselect through filters. In contrast, our study leverages the full dataset of 332 semiconductors to identify trends, distinguish desirable *n*-type and *p*-type characteristics for half-Heuslers, and establish statistical links to promising elemental subspaces. Our analysis reveals that excellent *n*-type performance is associated with compounds featuring ultra-high mobility at conduction band edges, while strong *p*-type behavior stems from high band degeneracy. We further demonstrate that elemental subspaces statistically linked to high β reinforce underlying physical design principles, leading us to identify four promising, yet underexplored subspaces for thermoelectric materials discovery. These include two primary subspaces of (i) yttrium- and (ii) zirconium-containing chemistries, along with two secondary subspaces for (iii) gold- and (iv) iridium-containing chemistries. Guided by these element-based recommendations, we present experimental work on rare earth gold stannides which yields ultra-low thermal conductivity half-Heusler alloys.

2 Methods

2.1 Chemical Replacements

In order to methodically consider an expansive variety of theoretical half-Heusler compounds, all elements with known electronegativities from groups 3 to 17 were utilized as possible inputs to the half-Heusler structure (Figure 1b). Transition metals were split between groups 3-7 and groups 8-12, with the former as chemical replacements for half-Heusler atom A and the latter groups' elements as atom B. An important constraint applied to this work was the requirement of a net 18 valence electrons per half-Heusler system. In such systems, atom A acts as a cation and donates all of its valence electrons to the covalently bonded and anionic BC pair. When these elements share and transfer electrons in this manner and with a net 18 valence electron count, the half-Heusler $A^{n+}(BC)^{n-}$ has a completely filled d-shell. This gap in energies before the next available orbital contributes to the likelihood of 18 valence electron half-Heuslers being semiconductors - a necessity for thermoelectric applications.^{2,3,35} This 18 electron constraint in combination with the groups of elements considered led to an initial pool 1,126 half-Heuslers for this work.

2.2 Structural Relaxation and Electronic Properties

First-principles calculations were performed with density functional theory (DFT) using the Vienna Ab Initio Simulation Package (VASP)³⁶ with Projector Augmented Wave (PAW) pseudopotentials.³⁷ The Perdew-Burke-Ernzerhof (PBE)³⁸ exchange correlation functional was used for structural relaxation. A plane wave cut off of 400 eV was utilized on a 8x8x8 Monkhorst-Pack sampled k-grid for relaxation. The total energy and total force convergence criteria for structural relaxations were 10^{-5} eV and 0.01 eV/Å respectively.

The PBE exchange-correlation functional as well as the Modified-Becke-Johnson (mBJ) meta-GGA functional²⁶ were utilized to evaluate band structure along a high-symmetry k-points path. Band gaps were analyzed from the results of both of these functionals, and the results of the mBJ band structure were kept in cases where only the PBE band gap closed but the mBJ gap did not. A high density k-grid, 14x14x14 Γ -centered, was utilized in order to converge electronic properties for trends analysis across all half-Heuslers calculated to have a band gap. Such calculations also utilized total energy criteria of 10^{-5} eV and total force convergence criteria of 0.01 eV/Å.

2.3 Thermoelectric Quality Factor

$$\beta \propto \frac{\mu_0 m_{DOS}^*{}^{3/2}}{\kappa_L} T^{5/2} \quad (1)$$

Thermoelectric quality factor, β , is a strong indicator of intrinsic thermoelectric performance.²⁰ As seen in Equation (1), β is directly evaluated from the ratio of electronic transport parameters to lattice thermal conductivity, where μ_0 is the intrinsic carrier charge mobility, m_{DOS}^* is the density of states (DOS) effective mass, κ_L is the lattice thermal conductivity and T is temperature. Intrinsic carrier charge mobility is evaluated from a semi-empirical model utilizing m_{DOS} , band degeneracy, and bulk mod-

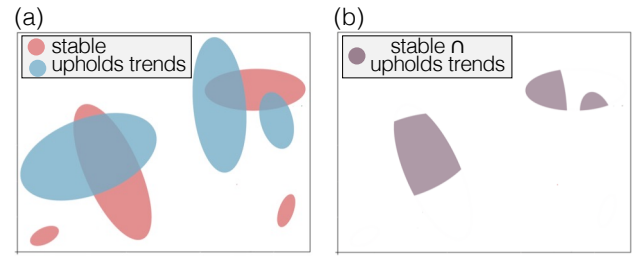


Fig. 2 Half-Heusler subspaces of interest are identified by (a) identifying chemical spaces associated with physical, interpretable trends (blue) and chemical spaces that harbor stable compounds (pink). (b) The intersection of these regions defines a unique and promising elemental sub-space.

ulus.²⁰ m_{DOS} is evaluated utilizing the density of states from a high k-point density DFT calculation as described in Section 2.2 and using a single parabolic band approximation. Bulk modulus is evaluated by fitting the Birch-Murnaghan equation of state.³⁹ κ_L is also evaluated from a semi-empirical model, and uses bulk modulus, number of atoms in the primitive unit cell, density, volume, mass, and average coordination number as inputs.¹⁹

2.4 Phase Stability

The thermodynamic stabilities of 332 half-Heuslers with band gaps were evaluated against all competing ternaries and binaries available on the Inorganic Crystal Structure Database (ICSD)⁴ through convex hull analysis. Due to the half-Heusler space being largely unexplored experimentally, some compounds had no known competing binaries. In these cases lowest energy competing phases from Materials Project (MP) were used to construct a convex hull. The lowest-energy elemental phase structures from MP were also retrieved for each compound.

Total energy calculations were performed for all competing phases. The majority of parameters for these calculations were generated from Pymatgen's MPRelaxSet,⁴⁰ but the energy convergence criteria was lowered to 10^{-6} eV and a total force convergence criteria of 0.01 eV/Å (as used in our geometry optimizations described in Section 2.2) was added. Compounds directly on the hull (distance = 0 eV) were marked as stable and compounds off the hull were marked to be unstable. Ranges of chemical potentials for which the predicted stable compounds remain stable were found by visualizing each stable system in chemical potential space.

2.5 Synthesis

The samples of ScAuSn, LuAuSn and $Sc_{0.5}Lu_{0.5}AuSn$ were prepared first using arc-melting of constituent elements (Sc 99.8%, Lu 99.9%, Au 99.99%, Sn 99.99%) under an ultra-pure argon atmosphere. The ingots were remelted and flipped several times to ensure homogeneity. The arc-melted materials were subsequently ground using an agate mortar and sintered in the induction hot press with conditions 700°C, 40 MPa, 15 min for ScAuSn and 625 °C, 40 MPa, 60-90 min for LuAuSn and $Sc_{0.5}Lu_{0.5}AuSn$.

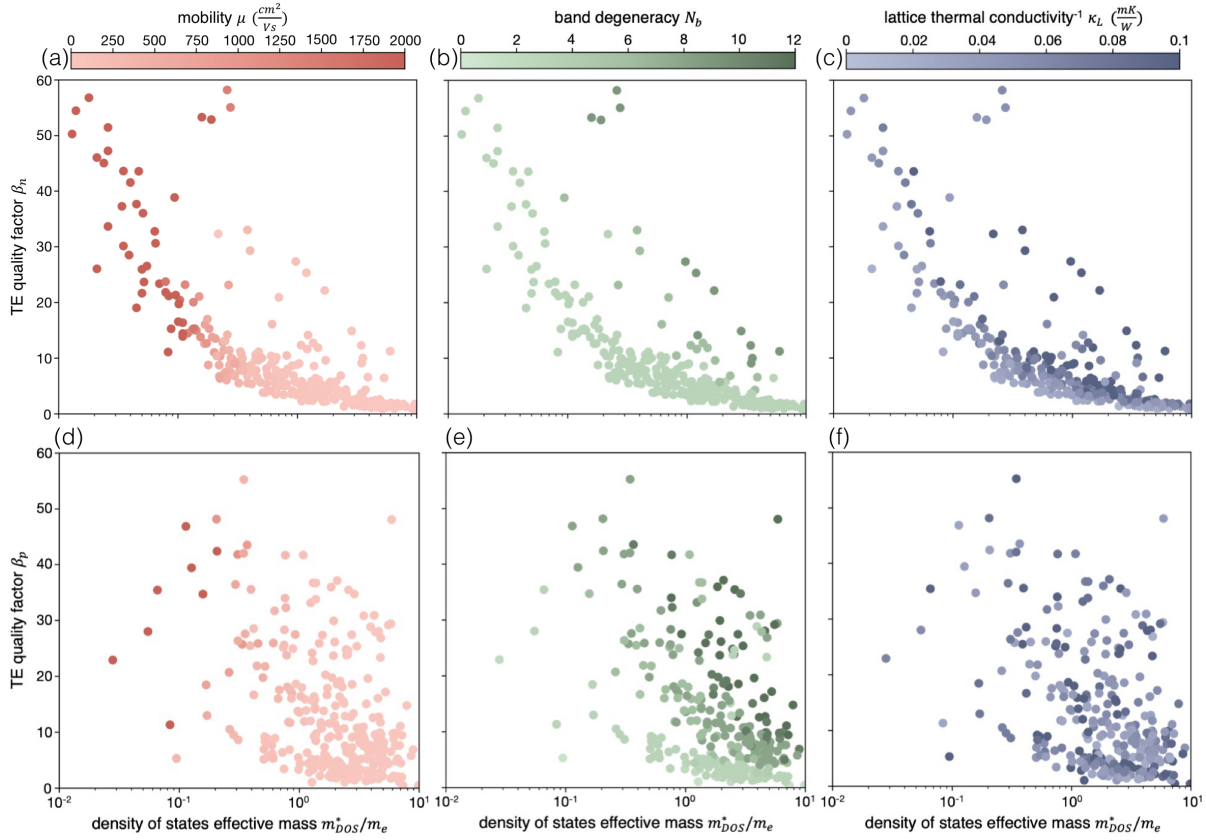


Fig. 3 When thermoelectric figure of merit, β , is visualized with respect to its components, distinct trends emerge for n -type and p -type performance. For n -type materials, a) high β values occur exclusively at low m_{DOS} and high electron mobility. b) As their band edge degeneracy is almost always fixed at $N_b = 3$, high β compounds must consistently exhibit low band mass m^*b . c) For a given m_{DOS} , compounds with lower lattice thermal conductivity achieve higher β . For p -type materials, d) the highest β values are less concentrated at lower m_{DOS} . e) Valence band degeneracy, particularly combined with low m_b^* at the valence band edge, correlates strongly with high β_p . e) While the lowest performing compounds tend to have the highest κ_L , the p -type association between κ_L and β_p is also less pronounced than in n -type.

2.6 Measurement

Crystal structure was studied with X-ray diffraction using a Bruker D2 Phaser device with a Cu radiation source. Rietveld refinement was performed with FullProf software. Density was measured with geometrical methods; for all the samples the values were $\sim 90\%$ or higher. The resistivity and Hall effect were studied on a custom-built apparatus⁴¹ using the Van der Pauw technique. The current supplied was 150 mA, while the magnetic field amounted to 1 T. Seebeck coefficient was also studied on a home-built apparatus⁴². Thermal conductivity was calculated from relation $\kappa = dC_pD$, where d stands for the density, C_p denotes heat capacity approximated from the Dulong-Petit law, while D is the diffusivity coefficient measured with the commercial Netzsch 467 apparatus. Throughout the analysis, lattice thermal conductivity was obtained using the Franz-Wiedemann law, where the Lorenz number was calculated as shown in Ref.⁴³.

3 Results and Discussion

3.1 Trends in Transport and Thermoelectric Quality Factor

To identify the features of half-Heuslers associated with promising performance, Figure 3 highlights several key trends observed in our computational dataset for both n -type and p -type performance. These trends are based on the 332 half-Heuslers (out

of a total of 1,126) that exhibit a non-zero band gap (see Section 2.2). As described by Equation 1, high intrinsic mobilities (μ_o), large density of states (DOS) effective masses (m_{DOS}^*), and low lattice thermal conductivities (κ_L) are desirable for achieving a high thermoelectric (TE) quality factor. However, the expression for β conceals additional complexities. DOS effective masses and mobilities are interconnected and influenced by band effective masses and band degeneracies. Optimally, a large DOS effective mass is achieved through multiple bands (high degeneracy) with low effective masses, which helps preserve high carrier mobilities, rather than by a single, heavy band. To explore these interdependencies, Figure 3 systematically examines pairwise relationships, offering insights that can guide the identification of promising subspaces. Correlation matrices of both n - and p -type data corresponding to Figure 3 is available in Figure S2 of the ESI.

Figure 3a illustrates the variation of β_n with the DOS effective mass. The data reveal an inverse relationship, where high DOS effective masses correspond to lower thermoelectric (TE) quality factors. Notably, the highest β values are observed in compounds with the lowest DOS effective masses. Each point in Figure 3a is shaded based on the calculated electron mobility (μ_e), highlighting that compounds with low m_{DOS}^* but high β_n achieve their

superior predicted performance due to exceptionally high electron mobilities. Figure 3b also plots β_n against the DOS effective mass, here with points colored by the band degeneracy (N_b) at the conduction band edge, with nearly the entire dataset sharing a degeneracy of 3. This visualization reveals that the high mobilities are linked to small band effective masses, as lower m_{DOS}^* must come from a small (m_b^*) given fixed N_b .

These trends can be further understood through the common structural features of half-Heusler conduction bands: the placement of the conduction band minimum (CBM) at the point X of the fcc lattice Brillouin zone, coupled with strongly curved bands.^{1,44} The CBM placement limits the *n*-type band degeneracy to 3, the multiplicity of the X point in the first Brillouin zone, or a theoretical maximum of 9 if each ion contributes an equivalent band at that point.^{35,44} As seen in Figure 3b, 286 of the 332 semiconductors considered here exhibit a total conduction band degeneracy of 3 (see Table S1 of the ESI). This is much lower than the degeneracies seen in *p*-type half Heuslers (Figure 3e). This limitation implies that achieving a high DOS effective mass – often regarded as beneficial for maximizing the thermoelectric quality factor β – in practice necessitates a large band effective mass and hinders mobility. Consequently, low DOS and band effective masses emerge as the primary, intertwined factors correlating with higher β for *n*-type performance.

To examine the influence of lattice thermal conductivity κ_L on predicted quality factor β_n , Figure 3c once again plots β_n against m_{DOS}^* , this time with compounds color-coded by the inverse of their predicted lattice thermal conductivity, with darker colors corresponding to lower κ_L . Achieving low lattice thermal conductivity in half-Heuslers is a well-documented challenge,^{45–47} and our computational results reflect this difficulty. The predicted κ_L values span a wide range, from 0.2 to 98 W/mK, with a median of 18 W/mK and first and third quartiles at 12 and 26 W/mK, respectively. These values contrast starkly with the < 1 W/mK achieved by state-of-the-art thermoelectric materials above room temperature. It is worthwhile to explore how this range of κ_L impacts the observed trends. Figure 3c shows that, for a given DOS effective mass, higher β_n values are generally associated with lower lattice thermal conductivities. The lighter color band, corresponding to compounds with relatively high κ_L , forms an envelope beneath the data points. As κ_L decreases (indicated by darker colors), the data points shift away from this envelope toward higher β_n .

Unlike *n*-type thermoelectric (TE) quality factors, *p*-type performance reveals much weaker correlations between β_p and the valence band DOS effective mass (m_{DOS}^*). Hole mobility (Figure 3d) is much more limited than that of electrons in *n*-type systems. Instead, Figure 3e indicates that high β can be achieved by higher DOS masses arising from high band degeneracy. Additionally, the highest lattice thermal conductivities (Figure 3f) tend to be paired with low β_n , but the distinct layers of higher TE quality factor seen with lower κ_L in *n*-type are not carried over in *p*-type. Rather, Figure 3d reveals that high β_p values are most strongly associated with small band effective masses combined with large valence band degeneracies as predictors of good performance.

The significance of band degeneracy for *p*-type performance can also be traced to the characteristics of half-Heusler band

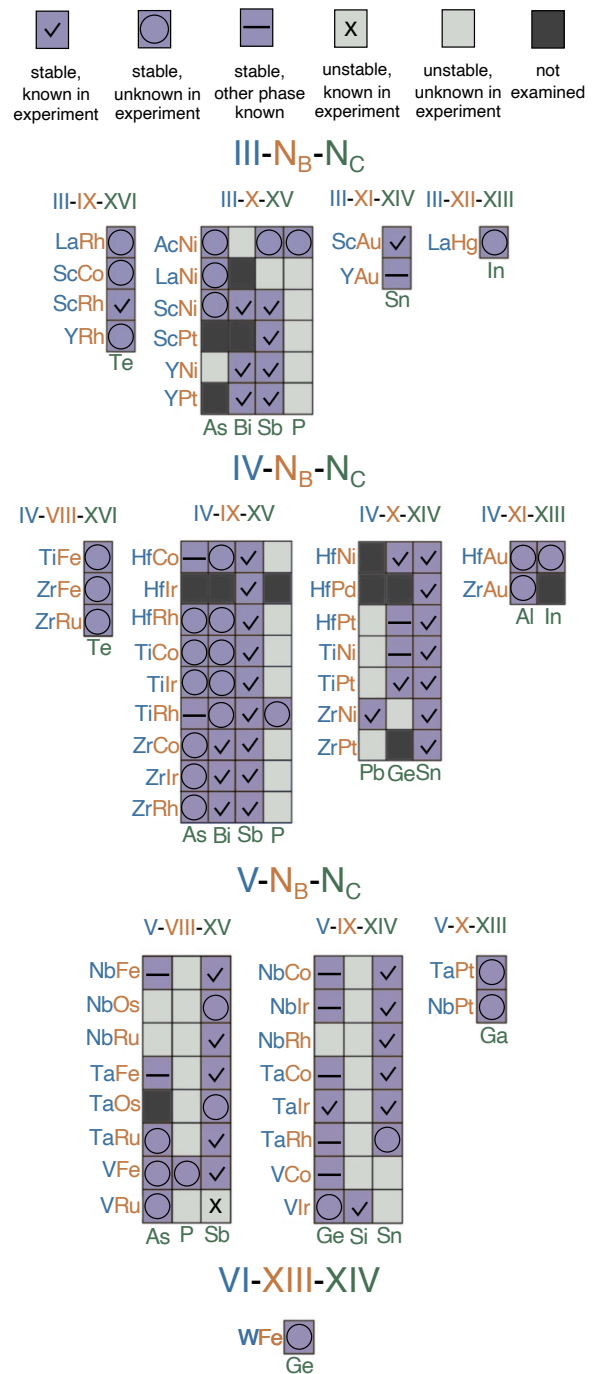


Fig. 4 Subset of 332 semiconductors analyzed for phase stability, including all 93 compounds predicted to be thermodynamically stable. Purple blocks represent compounds calculated to lie on the convex hull, those with checkmarks are experimentally known and those with circles are unreported in experiment. Purple blocks with horizontal lines indicate half-Heuslers predicted stable in this work but experimentally realized in another structure. Light grey blocks correspond to compounds that lie off the calculated convex hull. Dark grey blocks indicate compounds that were not considered for stability analysis.

structures. While the conduction band minimum (CBM) is consistently located at the point X, the valence band maximum (VBM) can occur at Γ , W, or L within the first Brillouin zone.^{1,48} This diversity in band edge placement, combined with the higher mul-

tiplicities of W and L (6 and 4, respectively) compared to X (3), allows for a broader range of band degeneracies in the valence band (see Table S2 in the ESI), especially when multiple of these extrema lie close in energy (see Figure S1). As a result, the p -type data encompass several categories: compounds with high DOS effective masses enabled by high valence band degeneracies but still maintaining low band effective masses, compounds with low DOS effective masses due to low valence band degeneracies but similarly low band effective masses, and a spectrum of intermediate DOS effective mass compounds. Figure 3e illustrates increasingly higher layers of β_p that can be achieved for a given DOS effective mass as valence band degeneracy increases.

Overall, this analysis yields distinct design rules for identifying promising chemical subspaces for n - and p -type performance. For n -type, we seek materials with sharp conduction band edges that yield low band effective mass and therefore high mobility. For p -type, we look for materials with high valence band degeneracy characterized by degenerate energy eigenstates across any of the Γ , W , or L points of the Brillouin zone. Such degeneracy, when coupled with steeper band edges when feasible, achieves high β_p . For both carrier types, we further seek compounds with lower κ_L where possible, as this can only increase TE quality factor β more. Below, we utilize these design rules across all calculated half-Heusler semiconductors to inform subspace identification.

3.2 Phase Stability

With an understanding of desirable transport properties for n - and p -type established, we next carry out phase stability analysis across the full space of 332 semiconducting half-Heuslers. We use convex hull analyses of all 332 semiconductors (as described in Section 2.4) from computed formation energies, and visualize the predicted compounds' stability in chemical potential space. The convex hull represents the lower envelope of phases that appear when phase formation energies are plotted as a function of composition. Phases that lie on the hull are thermodynamically stable, while those that lie above it are unstable or metastable. Analyses of hulls help identify which phases are stable within a chemical composition space, and the nearby competing phases.

A summary of all half-Heusler chemistries that lie on the convex hull is presented in Figure 4. Figure 4 is organized into 4 groups of $N_A - N_B - N_C$, where N refers to the group number of the periodic table shared between elements A, B, or C. The chemistries are first organized by the group number of element A, then B, and finally C. Compounds not included in Figure 4 are predicted to be unstable. Of the 332 half-Heuslers considered, 93 (marked in gold blocks) are predicted to be stable. We note that the 12 compounds marked as "stable, other phase known" were predicted to be thermodynamically stable here as half-Heuslers, but are only experimentally known in other phases (several are predicted stable in other studies as well⁴). These compounds may be false positives; alternatively targeted synthesis strategies may be effective for ultimately realizing them. Additionally, we note one false negative result: VRuSb, calculated as unstable but experimentally known as a half-Heusler.

There are 38 chemistries that are not experimentally known but

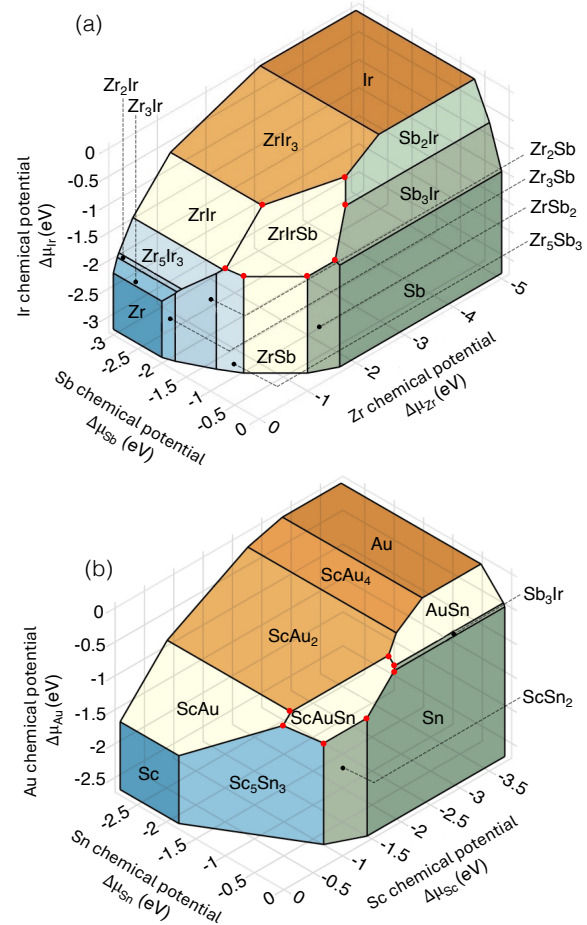


Fig. 5 Phase stability diagram of a) ZrIrSb and b) ScAuSn. Blue faces correspond to competing phases closest in composition to A-element, orange faces correspond to competing phases closest to B-element, and green faces correspond to competing phases closest in composition to C-element Bi. The red dots mark the invariant points at which the Half-Heusler is in equilibrium with competing phases.

predicted here to be stable labeled as "stable, unknown in experiment". While computational analyses of their properties exist, the majority of their thermodynamic stabilities had not been previously assessed; here, they are predicted to be stable and our findings align with existing computational literature where available. This label also includes 6 chemistries not reported in the literature either experimentally or computationally: YRbTe, AcNiAs, AcNiSb, AcNiP, HfAuIn, and LaHgIn. These predicted compounds are sparsely distributed throughout the chemical space, but reflect comparatively less explored chemical trends, such as actinide containing, B-site gold containing, or atypical p-block elements such as Te, In, and P.

It is interesting to analyze trends across the stability analysis, to provide an understanding of the chemistries that tend to be stable and those that do not. For example, in Figure 4 the block IV-IX-XV appears to be heavily explored and largely composed of stable compounds including well-known thermoelectric half-Heuslers HfCoSb and ZrIrSb. Across multiple blocks, we see that nearly all Sb-containing half-Heuslers are stable, and also have

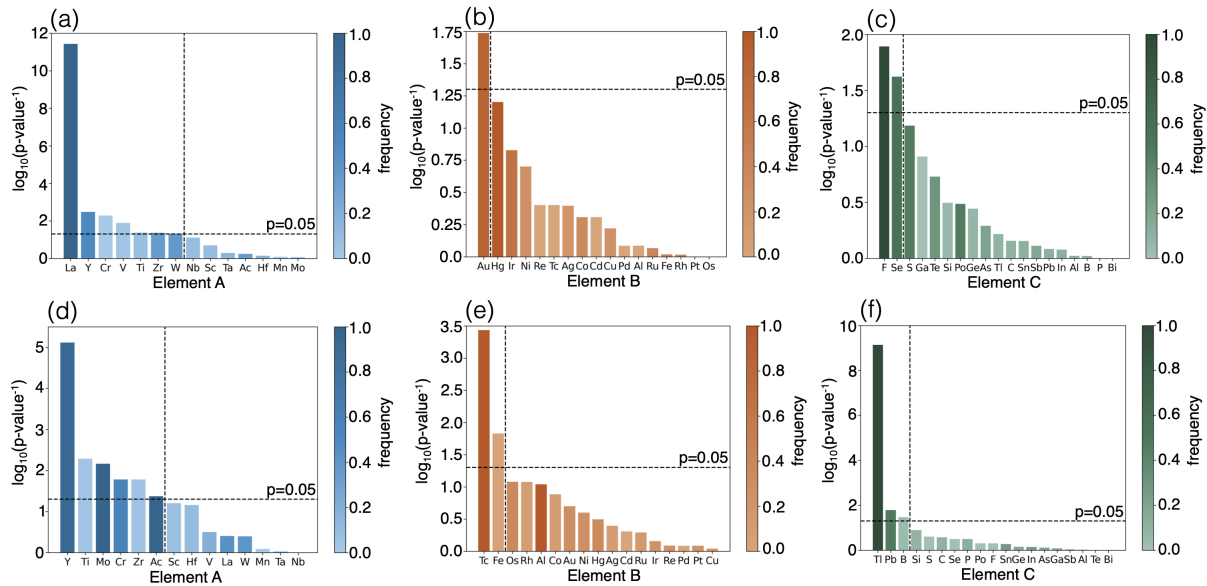


Fig. 6 Statistical analysis results using Barnard's exact test. Frequency coloring represents the proportion of times an element was associated with high β values. The y-axis shows $\log_{10}(1/p)$, so that the statistically significant elements yield the largest bars. Subfigures (a), (b), and (c) show n -type data for A, B, and C elements, respectively, while subfigures (d), (e), and (f) present p -type data for the same groups. Horizontal lines denote the significance threshold (0.05), and vertical lines mark the cutoff beyond which elements are not statistically significant.

been previously reported in the literature.

It is also interesting to understand the compounds that are predicted to be unstable, given the goal of identifying comparatively underexplored but promising subspaces that contain realizable chemistries. For instance, Figure 4 shows that chemistries with C-elements P, Pb, or Si often lie off the convex hull. This instability frequently arises from competing 1:1:1 stoichiometric phases, typically in the orthorhombic $Pnma$ structure. Examples include ScNiP and TaCoSi , which have higher formation energies than their experimentally known $Pnma$ counterparts⁴. Additionally, LaNiP and YNiP remain off the convex hull due to hexagonal $P63/Mmc$ phases, while YPtP has a more favorable ternary in hexagonal $P6m2$.

As for the unstable group of Pb-based compounds seen in Figure 4, here we often observe a competing AB binary. Favorable compounds HfPt , TiNi , TiPt , and ZrPt effectively exclude HfPtPb , TiNiPb , TiPtPb , and ZrPtPb respectively from the convex hull. In comparison, these competing AB-element binaries exhibit higher formation energies for largely stable groups of half-Heuslers such as the IV-IX-XV group.

Figure 5 shows two example stable chemistries, ZrIrSb and ScAuSn , visualized in chemical potential space. In chemical potential space, a chemical potential of element i , $\Delta\mu_i$, that is closer to 0 indicates element i -rich conditions while a more negative $\Delta\mu_i$ value indicates element i -poor conditions. This visualization gives further insight to the stability of each predicted-stable compound, including the bounding phases and the thermodynamic conditions under which it may be likely to form.

3.3 Subspace Identification

3.3.1 Statistical Testing.

To begin identifying promising subspaces within half-Heusler chemistries, Barnard's exact test was applied to evaluate correlations between specific elements in the A, B, or C sublattices and TE quality factor β . Known for its precision in small-sample comparisons, Barnard's test provides robust insights into specific elements most strongly associated with high or low β and therefore TE behavior. Alternative statistical methods were attempted but ultimately deemed unsuitable due to specific limitations. For example, chi-squared and Mutual Information tests require larger sample sizes (e.g., $n > 1000$, compared to our dataset of 332 semiconductors), and ANOVA assumes linear trends and homogeneous variance between groups, which do not align with our data. Fisher's exact test, though designed for small sample sizes, was also excluded because it conditions only on contingency tables with fixed marginal totals, unlike Barnard's test, which considers all possible tables.

Barnard's test was performed on all A, B, and C elements from the list of half-Heuslers predicted to exhibit a non-zero band gap. As the test requires categorical data, compounds were classified as "high" or "low" β for n -type and p -type materials. High β values were defined as those in the top 20%, with the remainder categorized as low. The p-values for each element are shown in Figure 6, where bar shading indicates the frequency with which compounds containing each element are classified as high β . The significance threshold for associations was set at $p=0.05$.

The analysis reveals several elements that achieve statistical significance in their associations with β . For n -type thermoelectrics, the A-elements La, Y, Cr, V, Ti, Zr, and W show significant p-values (Figure 6a), while Au among the B-elements (Figure 6b) and F and Se among the C-elements (Figure 6c) also stand

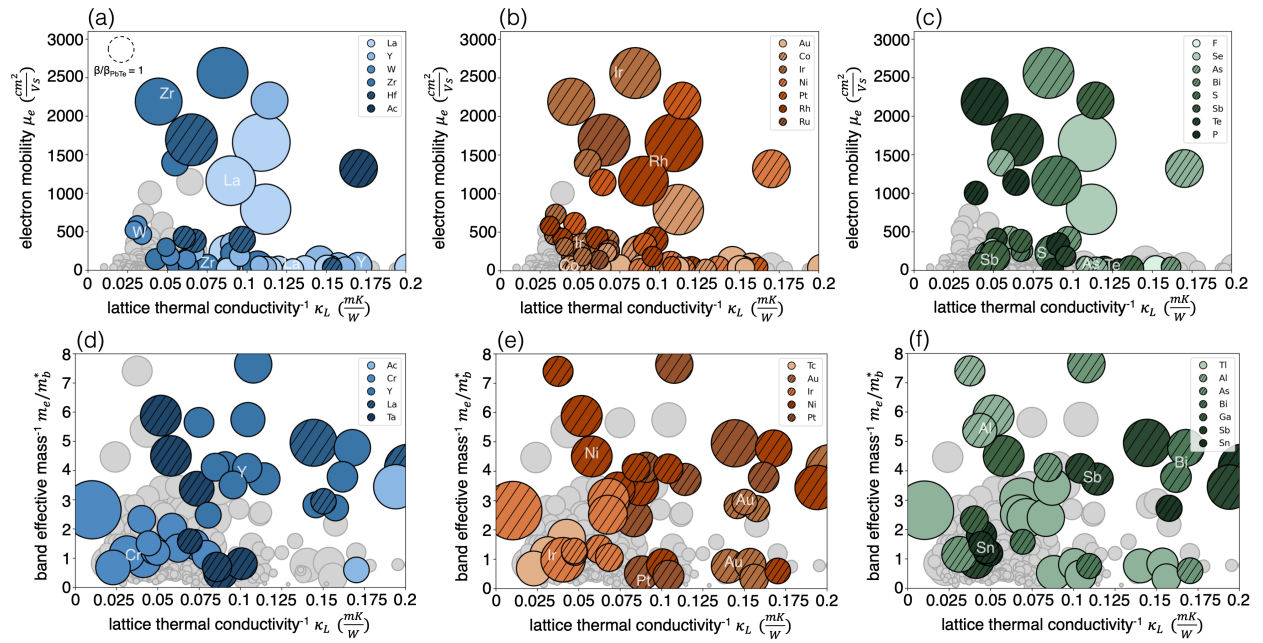


Fig. 7 Visualization of the distribution of transport properties among all 332 half-Heusler semiconductors. Half heusler n -type performance is visualized by (a) A-element, (b) B-element, and (c) C-element, and p -type performance is also visualized by (d) A-element (e) B-element and (f) C-element. Marker size corresponds to value of TE quality factor β , a reference to classic TE material PbTe is supplied in (a). Compounds with predicted values of β in the top 20% are marked in color, while lower β value compounds are marked in gray. The top 20% compounds contain many of the elements that show statistical significance (shaded) as well as additional elements (shaded and cross-hatched).

out. In p -type materials, significant A-elements include Y, Ti, Mo, Cr, Zr, and Ac (Figure 6d); significant B-elements are Tc and Fe (Figure 6e); and significant C-elements are Tl, Pb, and B (Figure 6f).

It is essential to note that Barnard's exact test identifies significant associations but does not inherently indicate the direction of these correlations (i.e., whether an element is associated with high or low β). To address this, the proportion of high- β versus low- β compounds within each element's contingency table was examined, and only elements with a stronger association to high β were retained for further analysis. These elements are represented by darker bars in Figure 6. For n -type performance, the most significant A-elements then become La, Y, Zr, and W; Au is the significant B-element; and F and Se are significant C-elements. For p -type performance, significant A-elements are Y, Mo, Cr, and Ac; Tc is the significant B-element; and Tl and Pb emerge as significant C-elements. By contrast, elements such as Cr, V, and Ti for n -type, and Ti, Zr, Fe, and B for p -type, are excluded as their light shading indicates stronger correlations with low β .

We note that Figure 6 shows the presence of elements frequently associated with high β values but without statistically significant p-values. For example, Hg and Ir as B elements, and S and Po as C element for n -type (Figure 6b,c), and Al as B element for p -type (Figure 6e) exhibit this behavior. The most common explanation for this behavior is that, although these chemistries correlate with high β , they are typically associated with small sample sizes. Their infrequent occurrence within the dataset results in greater variability and reduced statistical power. Consequently, their associations with high β are less likely to achieve

significance in Figure 6 despite their apparent relevance.

Lastly, we note that subspaces defined by descriptors other than elemental species are also viable in principle. For example, we examined subspaces based on elemental group numbers and group number differences (Figure S3 in the ESI). However, these groupings do not exhibit the strong correlations observed in the element-specific perspective. Although alternative descriptors may exist, the pronounced trends in elemental chemistry – and their connection to underlying physical insights (see next subsection) – support the focus on element-based subspaces here. A key advantage of these subspaces is the direct identification of promising elements, which can then be targeted for alloying strategies, as alloyed half-Heuslers have demonstrated the highest thermoelectric potential to date. However, it is important to acknowledge that not all physical properties or performance factors can be fully captured through elemental subspaces alone, highlighting the potential need for additional refinement or complementary descriptors in future studies.

3.3.2 Applying Transport Trends to Significant Elements.

Next, we analyze the elements frequently found in high- β compounds and their overlap with the statistically significant elements identified by Barnard's exact test. While Barnard's test evaluates whether the presence of a specific element increases the likelihood of high performance, this analysis identifies the elements most likely to be present in a high-performing compound. Additionally, we assess whether these elements align with the transport trends established in Section 3.1. This approach ensures the observed correlations reflect reproducible and interpretable physical mechanisms that offer meaningful insights into

transport behavior.

Figure 7 provides a detailed visualization of the transport trends identified in Figure 3. Each marker represents a compound, with marker size corresponding to the magnitude of quality factor β . Colored markers denote elements frequently appearing in the top 20%, while gray markers represent elements that are either infrequent in the top 20% or associated with lower-performing compounds outside this range. Solid colored markers denote frequent elements that were also identified as statistically significant with Barnard's test, while cross-hatched markers highlight frequent elements not identified as statistically significant. Notably, the elements identified as frequently occurring in the top 20% overlap substantially with those found using Barnard's exact test.

In Figure 7, panels (a-c) illustrate the predicted *n*-type trend, where high electron mobility and low lattice thermal conductivity drive superior thermoelectric (TE) performance. As expected, the highest-performing compounds are clustered in the upper-right corner. Panels (d-f) depict the *p*-type trend, highlighting the roles of low band mass, low lattice thermal conductivity, and high band degeneracy. The broader distribution of the largest markers in Figure 7(d-f) reflects the influence of band degeneracy, which allows high β values to arise across the parameter space rather than being confined to the upper-right corner. Even so, Figure 7d contains a series of yttrium-based compounds, all sharing the same degeneracy, that consistently achieve higher β values as they progress from the lower left to the upper right.

An important takeaway from Figure 7 is that the statistically significant A elements identified in Figure 6 dominate the top 20% of compounds for both *n*-type and *p*-type half-Heuslers (Figure 7(a,d)), as indicated by the prevalence of solid colored markers over cross-hatched ones. Combined with the higher prevalence of significant A elements compared to B and C elements (Figure 6), these findings suggest that TE performance is most strongly driven by the A element. In contrast, the top-performing compounds exhibit greater variability in B and C elements, suggesting a lesser role. Further, the significant B and C elements from Figure 6 account for a smaller fraction of the top-performing compounds (Figure 7(b,c,e,f)). The prominence of the A element likely arises from its unique role in orbital hybridization. While B and C atoms form a covalently bonded zinc blende sublattice acting as an effective anion (see Section 2.1), the A element retains much of its elemental character, allowing it to exert greater influence.

Considering *n*-type semiconductors in detail, all elements that were identified as statistically significant and associated with high β are found in Figure 7(a-c): A-elements La, Y, W, and Zr; B-element Au, and the C-elements F and Se. Additional elements (marked with cross-hatching) also appear frequently in high β compounds. These additional elements fall into two main categories: (i) elements present in a significant proportion of top 20% β compounds but also frequently found in low β compounds, and (ii) elements that were frequently associated with high β values in statistical testing but lacked sufficient data to achieve statistically significant *p*-values. For most cross-hatched elements, their presence in the top-performing compounds seems incidental, as

many poor-performing compounds also contain these elements (case (i)). An exception we identified is Ir, which, as a B-element, consistently contributes to high β values due to its exceptionally high electron mobilities. However, Ir was not identified as statistically significant in Barnard's exact test due to its small representation in the dataset (case (ii)), despite its strong association with high β compounds.

Considering *p*-type semiconductors in detail, again elements that were identified as statistically significant and associated with high β are found in Figure 7(d-f). Many additional elements appear frequently in the top performing *p*-type compounds as well. As in *n*-type, the prevalence of these elements in poor TEs made these non-statistically significant with Barnard's test. Here Au and again Ir are exceptions, achieving uniquely high β_p in within the dataset. From Figure 7(e), Au-containing chemistries conform to the expected trends of low m_b^* and κ for optimizing *p*-type performance, while Ir-based half-Heuslers exhibit exceptionally high band degeneracy at the valence band edge.

The frequent appearance of Au and Ir in the top 20% of *p*-type compounds, despite their lack of statistical significance, is more complex to interpret. For Ir, the smaller sample size likely again contributes to this outcome. However, as shown by the shading of the Au and Ir bars in Figure 6e, these elements are not consistently associated with a high TE quality factor. Instead, a subset of Au and Ir compounds exhibits exceptionally high β values – Au due to low thermal conductivity combined with decent electronic transport, and Ir due to exceptionally high band degeneracies. These findings reflect that elemental subspaces alone do not fully capture all physical properties relevant to thermoelectric performance. The combination of Ir or Au with more nuanced features – such as degree of orbital hybridization, bonding characteristic (as characterized by COHP for instance), or other aspects of electronic structure – could yield insights into compounds with high β . Future studies may benefit from exploring hybrid subspaces that incorporate both elemental and other descriptors, to better understand the exceptional cases.

In summary, all elements identified as strongly associated with high β using Barnard's test align with the physical trends driving high performance in both *n*-type and *p*-type semiconductors and frequently appear in the top 20% of compounds. Specifically, for *n*-type, these include the A-elements La, Y, W, and Zr; the B-element Au; and the C-elements F and Se. For *p*-type, they are the A-elements Ac, Cr, and Y; the B-element Tc; and the C-element Tl. Among these, the A-element plays a particularly critical role in determining transport behavior, with its presence serving as a strong predictor of good thermoelectric performance. Additionally, Ir (for both *p*-type and *n*-type) and Au (for *p*-type) are noteworthy, as they frequently appear in the top 20% of performers, even though their presence alone does not consistently guarantee high predicted TE performance.

3.3.3 Filtering Elements by Stability.

The considerations above identify elemental spaces of interest from which our promising subspaces are to be selected. As the goal is to identify promising, element-based subspaces for utilizable half-Heuslers, we now incorporate the phase stability anal-

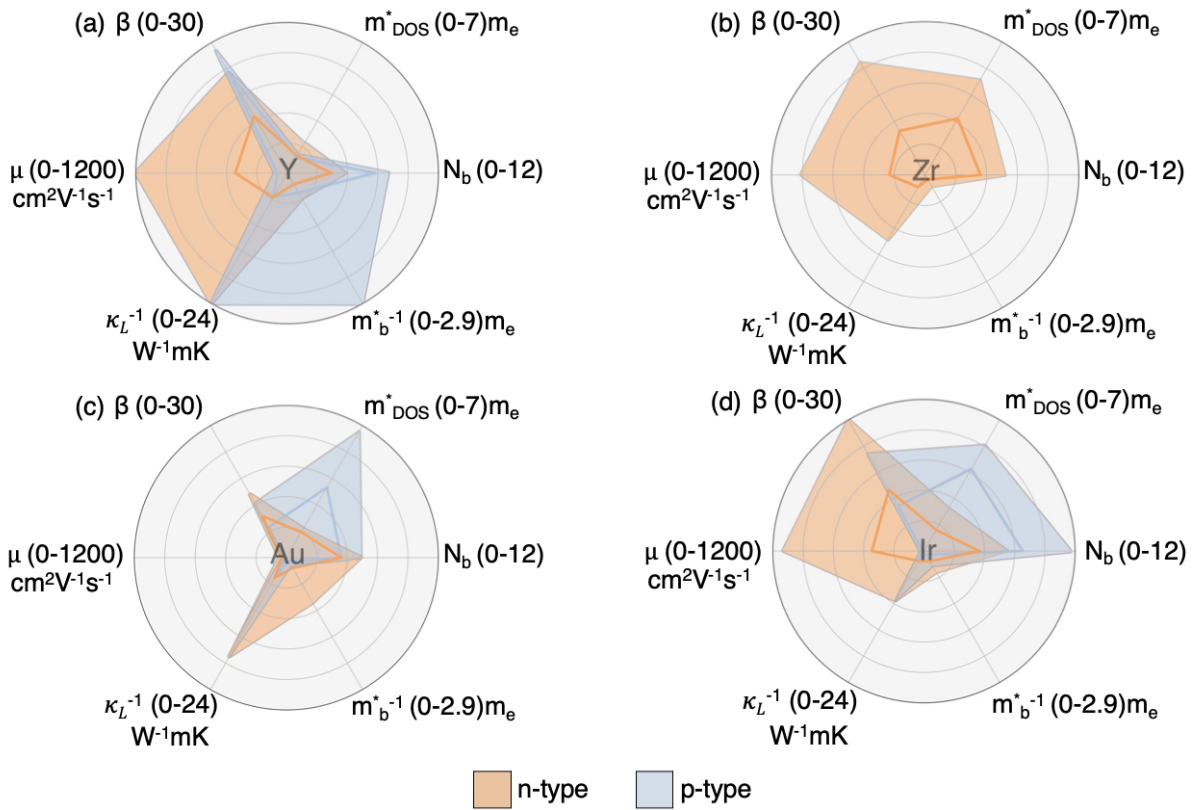


Fig. 8 Spider plot visualization of elemental subspaces: Primary subspaces are a) Yttrium containing chemistries, and b) Zirconium containing chemistries. Secondary subspaces are c) Gold, and d) Iridium containing chemistries. Different properties are plotted with respect to their relationship with β , so that maximum shading indicates higher performance. Blue corresponds to p -type performance and orange to n -type. Darker shaded lines are plotted along the average values and lighter shading indicates the standard deviation for all stable compounds considered containing that element.

ysis provided in Section 3.2. As shown in Figure 2, it is practically of interest to identify the overlap between areas that are promising in terms of their physical trends, and likely to yield stable compounds that are, when possible, in comparatively less explored regions of phase space.

In n -type, the consideration of physical trends (Figure 7(a-c)) in conjunction with stability analyses identifies a more refined set of elements. More specifically, La, W, F, and Se are removed from consideration due to their being part of very few stable chemistries – especially those that are not already extensively explored. This leaves A-elements Y and Zr along with Au as a B-element. In p -type (Figure 7(d-f)), Ac, Cr, Mo, Tc, Tl, and Pb are also removed due to yielding extremely limited stable chemistries (Figure 4); Ac, Tc, and Tl are also particularly less desirable by default given their toxicity and/or radioactivity. Thus, A-element Y demonstrates strong potential for superior TE performance in p -type as well. Finally, Au as a p -type element and Ir as both a p -type and n -type element are retained due to their presence in numerous stable chemistries. This refined selection highlights the balance between statistical significance, transport properties, and material stability.

3.3.4 Selection and Analysis of Promising Subspaces.

With clear insights into transport trends, key elements, and stability, we finalize the selection of promising subspaces for explo-

ration. The chosen subspaces are illustrated in Figure 8. *Primary subspaces* include A-elements Y and Zr (Figures 8a,b). Yttrium is featured for both n - and p -type performance due to its statistical significance in both categories, while zirconium focuses on n -type performance. In these primary subspaces, the presence of the element strongly correlates with high β , making them the most promising areas for investigation. *Secondary subspaces* include B-elements Au and Ir (Figures 8c,d) for both n - and p -type performance. Unlike primary subspaces, the presence of these elements does not always strongly correlate with high β (with n -type Au being a partial exception). Additionally, as B-elements, their influence is generally weaker compared to A-elements. However, they are noteworthy due to the existence of many Au- or Ir-containing compounds that demonstrate exceptionally high β values.

The visualization of these subspaces in Figure 8 embody key components of β that drive high TE performance in both n -type and p -type materials. Each subspace is summarized using data from all associated chemistries predicted to be thermodynamically stable. In the Y-based subspace, high β is driven by lower lattice thermal conductivity, a rare trait in half-Heusler desirable for TE efficiency (Figure 8a). As predicted, Y achieves superior electronic transport properties as a result of exceptionally high electron mobilities despite low DOS effective mass (n -type), and a combination of low band mass and high degeneracy for p -type. An advantage of Y is that it is predicted to be a high performance

subspace, independent of whether the material turns out to be natively n or p -type. For Zr, *n*-type β is again enhanced by particularly high electron mobility (Figure 8c). These primary subspaces form the basis for a range of high-performing thermoelectric materials.

The Au-based subspace, as anticipated for a secondary B-element subspace, demonstrates more modest overall statistics but includes notable standout properties. Half-Heuslers in the Au-based subspace, for example, show a low lattice thermal conductivity which benefits both carrier types. The interplay between a high DOS effective mass and low lattice thermal conductivity benefits *p*-type TE quality factor specifically, but the high DOS effective mass limits carrier mobility and adversely affects electronic transport (Figure 8c). Even so, its chemistries with particularly low lattice thermal conductivity exhibit some of the highest β values across the whole dataset. The Ir-based subspace stands out for its exceptionally high electron mobility in *n*-type applications, while *p*-type performance is once again driven by high band degeneracy. This nuanced understanding of how different elements influence TE performance enables a targeted approach to optimize chemistries for both *n*-type and *p*-type materials, while also guiding the intentional exploration of the most promising groups within the largely uncharacterized half-Heusler space.

3.4 Validation

In this section we gather experimental data from literature and compare to our theoretically selected subspaces. The selected subspaces not only encompass the top-performing chemistries computationally identified in this study, but also account for many known, top-performing half-Heuslers. For example, well-known *p*-type YNiSb and YPtSb fall into the yttrium-based half-Heusler phases highlighted for low thermal conductivity. Several of the representatives of this family have been reported with promising thermoelectric properties. YPtSb^{49–51}, YNiBi⁵², YNiSb⁵⁰, and YPdSb⁵⁰ exhibited in experiment low lattice thermal conductivities of 2-4 Wm⁻¹K¹ range, 2.5, 2.3, and 2.4 Wm⁻¹K⁻¹, respectively. These values are significantly lower than those for other well known half-Heusler thermoelectrics in their pristine form at 300 K, e.g. for ZrNiSn⁵³, TiNiSn⁵³, ZrCoBi³³, and VFeSb⁵⁴, which exhibit lattice thermal conductivity of 8-13 Wm⁻¹K⁻¹.

Reaching out to other properties, our calculations predicted extremely high mobility at 300 K for YPtSb: 2200 cm²/Vs. One of the experimental reports confirms the prediction within the order of magnitude, reporting even higher mobility at room temperature, 4000 cm²/Vs⁵⁵. Here, it is worth noting that other experimental reports for YPtSb indicate lower mobility (164 cm²/Vs⁴⁹ and 300 cm²/Vs⁵¹), which may stem from large susceptibility of transport properties to disorder, typical for half-Heusler compounds^{56–58}. When it comes to overall performance, YPtSb, for which one of the highest β is predicted here, was shown in experiment to have a zT of 0.6 at 1000 K in a single-sample study⁴⁹. This, in combination with our identification of yttrium subspaces, suggests that there may be additional promising materials to be identified in these subspaces, given efforts of optimization by doping, alloying and other more intricate techniques.

It is of interest to consider well-known TE materials not present in the selected subspaces, such as *n*-type NbCoSn and VFeSb. Although these compounds rank highly in our dataset, their high performance is an exception among typically low-performing chemistries based on the A-element. Conversely, some known compounds like *n*-type TaCoSn and *p*-type HfPtSn appear in the bottom third of our dataset when ranked. These discrepancies suggest that some compounds cannot be selected based solely on elemental subspaces and may require additional descriptors. Further, our computational analysis predicts idealized performance based on intrinsic properties, assuming optimal carrier type and concentration. Many of the known half-Heusler TEs may have been identified for their performance without targeted doping and optimization.

Our findings imply that higher performance may be achievable with less-explored species, provided carrier type and concentration are optimized. For example, while Zr compounds like ZrCoBi, ZrCoSb, and ZrPtSn are typically reported for *p*-type behavior, we predict high potential for *n*-type performance in Zr containing compounds. Specifically, we predict exceptional *n*-type performance for ZrIrSb, though achieving this will likely require specific synthesis and doping strategies. Figure 5(a) shows a large stability region for ZrIrSb, indicated a variety of thermodynamic environments under which the material may be synthesized. Promising synthesis strategies likely lie in cation-rich regions of phase space, near phase boundaries with ZrSb and Zr₅Sb₃, to suppress V_{Zr} and achieve optimal performance.

3.4.1 Our experimental studies

The above experimental considerations focus on prior results for yttrium pnictides with a transition metal from the tenth group of the periodic table (Ni, Pd, Pt). Our calculations similarly predict interesting properties for the less known group of rare-earth gold stannides (REAuSn), explored here as a testament to the chemistries encompassed by the subspaces identified in this work. While several Y- and Zr-based compounds are already known as decent thermoelectrics, e.g. ZrNiSn⁵⁶, ZrCoBi³³, YPtSb⁴⁹, YNiSb⁵⁹, the Au-subspace appears uncharted and further motivates our experimental exploration. Thus, from the Au-based secondary subspace, we anticipated uniquely low lattice thermal conductivity for REAuSn half-Heuslers.

We first synthesized ScAuSn, which we predicted to be a narrow band gap semiconductor ($E_g \approx 100$ meV, see Table S3) and stable (Figures 4 and 5b). The experimental low electrical resistivity and low Seebeck coefficient (Fig. 9b, c) are in concert with the predicted band structure. The measured room temperature mobility (ca. 30 cm²/Vs) is also within a factor of two of the theoretical value for the valence band (17 cm²/Vs). The lattice thermal conductivity for ScAuSn drops from 11 to 8 Wm⁻¹K⁻¹ from RT to 575 K, which is in agreement with our predicted value of 8 Wm⁻¹K⁻¹ at RT; see Figure 9d.

The next natural step would be an attempt to synthesize the heavier counterpart in the series of rare-earth gold stannides: YAuSn, thereby also incorporating Y from the primary subspace. For this material we predicted that, consistent with many other yttrium-bearing half-Heuslers, it will show ultra low lattice ther-

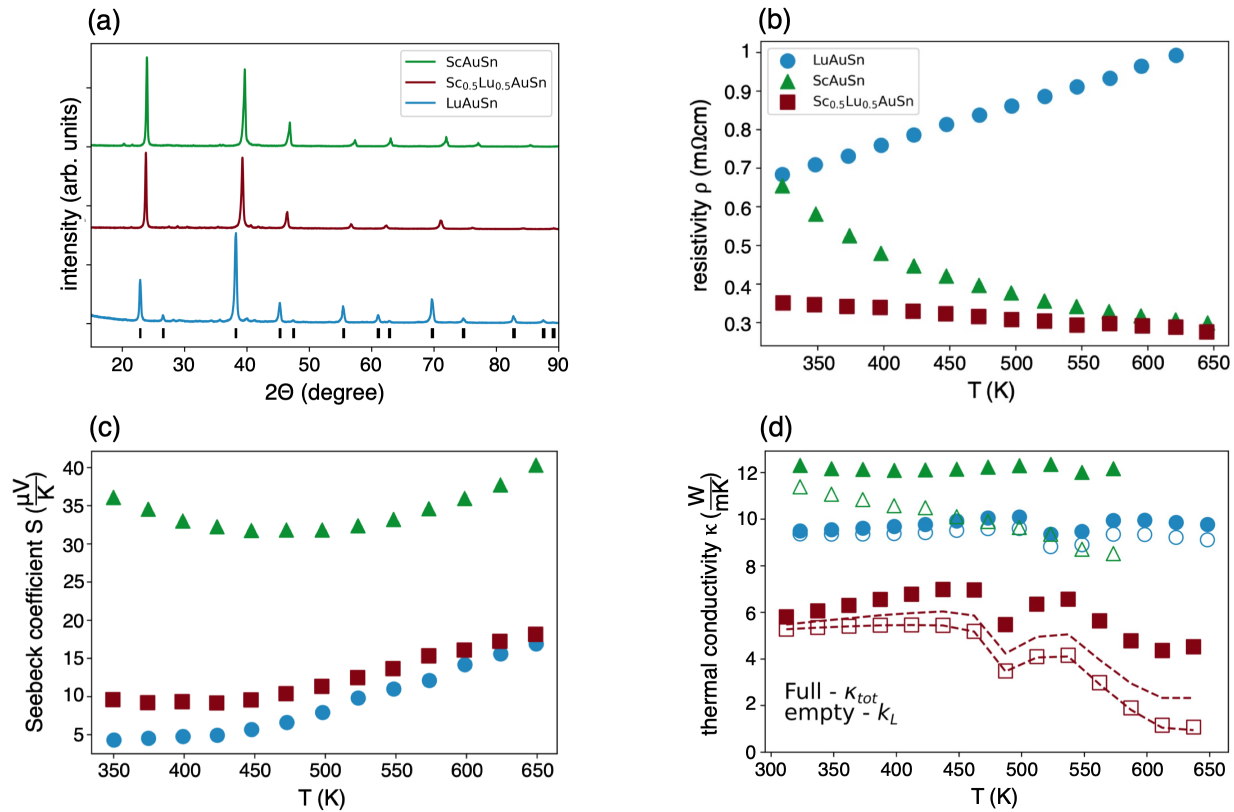


Fig. 9 Experimental studies of rare-earth gold stannides revealed ultra-low thermal conductivity. Panel (a) displays almost single-phase XRD; panel (b) demonstrates similar semimetallic resistivity for all the samples. $\text{Sc}_{0.5}\text{Lu}_{0.5}\text{AuSn}$ has the lowest ρ due to decent mobility and rather high carrier concentration, see Tab. 1. Panel (c) shows Seebeck coefficient, while (d) presents thermal conductivity - κ_{tot} with full symbols and κ_L with open symbols. Two dashed lines represent upper and lower limit of κ_L depending on Lorenz number (see text for details).

mal conductivity and good overall TE performance (ESI Tables S4). As indicated in Figure 4, although computationally predicted to be stable, experimentally this compound is known to crystallize in hexagonal symmetry (space group $P63mc$) instead of the half-Heusler structure.⁶⁰ Given that the two phases are energetically competitive, a targeted synthesis approach addressing the possible multi-phase behavior could be explored to stabilize the half-Heusler phase.

Fortunately, the heaviest rare-earth element (Lu) is able to substitute yttrium, leading to LuAuSn crystallizing in a half-Heusler structure.⁶⁰ Hence, we synthesized LuAuSn, and obtained a semimetal with carrier concentration even higher than for ScAuSn; see Table 1 for values of carrier concentration at RT and Figure 9b for resistivity. Accordingly, values of mobility at 300 K for LuAuSn are revealed to be rather low ($4 \text{ cm}^2/\text{Vs}$) compared to the Sc-based counterpart; *c.f.* Table 1. The lattice thermal conductivity showed a relatively steady value of $9 \text{ Wm}^{-1}\text{K}^{-1}$ between 300 K and 650 K (see Figure 9d).

In order to optimize the properties measured for each 1:1:1 chemistry and more fully characterize the promising REAuSn space, we took the opportunity of making a heavily strained alloy between the gold stannides: $\text{Sc}_{0.5}\text{Lu}_{0.5}\text{AuSn}$. The so-obtained material turned out to be single phase (see Figure 9a for XRD), with lattice parameter of 6.491 \AA — close to the average of the parent ternaries.⁶⁰ The carrier concentration was also close to the aver-

age values of ScAuSn and LuAuSn (Table 1). Interestingly, despite significant differences in masses and sizes between Sc and Lu, the mobility maintained relatively high values of $19 \text{ cm}^2/\text{Vs}$ at RT (Table 1). Most importantly, we observed strong suppression of phonon transport. When we used the standard procedure for calculating the Lorenz number from Seebeck coefficient⁴³, the lattice thermal conductivity dropped to $1.1 \text{ Wm}^{-1}\text{K}^{-1}$ at 650 K. This is an ultra-low value compared to other half-Heusler thermoelectrics, including many best performing compounds.^{61,62}

Here, however, it is worth noting that for $\text{Sc}_{0.5}\text{Lu}_{0.5}\text{AuSn}$ the majority contribution to thermal conductivity is coming from the electronic component. In systems of that kind, precise estimation of lattice thermal conductivity may be difficult due to imperfections of the Franz-Wiedemann Law, see e.g. Ref.⁶³. The Lorenz number generally is known to be in range $1.5\text{-}2.44 \times 10^{-8} \text{ W}\Omega\text{K}^2$.⁴³ The lower values are typical for intrinsic semiconductors. With increasing conductivity, the Lorenz number also increases; the top limit is relevant for metals.

To ensure transparency of our results, we calculated the upper and lower limit of κ_L , using the smallest and the largest available Lorenz numbers respectively. The range of possible κ_L values are visualized by dashed lines in Figure 9d. At the highest temperature of measurement, κ_L calculated as such ranges between $0.9 \text{ Wm}^{-1}\text{K}^{-1}$ and $2.3 \text{ Wm}^{-1}\text{K}^{-1}$.

To get a preliminary insight into the origin of this interesting

finding, we measured sound velocities (v_s). The results are displayed in Table 1 and reveal that rare-earth gold stannides show relatively low v_s , down to *ca.* 2200 m/s for LuAuSn and Sc_{0.5}Lu_{0.5}AuSn. This is indicative of soft bonding in the studied group. Here, it is worth mentioning that in recent years v_s values of 2800 m/s for ZrCoBi³³ and 2500 m/s for RNiSb compounds (R = Er, Tm, Lu)⁶⁴ were considered among the lowest for half-Heusler phases. In summary, we succeeded in obtaining ultra-low thermal conductivity due to point-defect disorder and extremely soft bonding for Sc_{0.5}Lu_{0.5}AuSn, as guided by the design rules and trends across chemistry identified in this work.

Table 1 Carrier concentration (n_H), Hall mobility (μ_H), and mean sound velocity (v_s) for the synthesized rare-earth stannides.

	n_H [1/cm ³]	μ_H [cm ² /Vs]	v_s [m/s]
ScAuSn	2.6×10^{20}	31	2906
Sc _{0.5} Lu _{0.5} AuSn	9.5×10^{20}	19	2191
LuAuSn	1.7×10^{21}	4	2217

4 Conclusions

In this study, we examine 332 semiconducting ABC half-Heusler compounds, analyzing their electronic structure, stability, and transport properties critical for optimal thermoelectric performance. Our modified screening approach emphasizes patterns across families of materials rather than relying on individual material predictions. This strategy is especially valuable for transport properties - derived from semi-empirical models at the high-throughput scale - and allows us to extract robust trends and link them to chemical composition for tuning half-Heusler properties.

Such trends yield insights into desirable properties for different polarity semiconductors. For *n*-type materials, we seek half-Heuslers with sharp conduction band edges that yield low band effective mass, which directly contributes to high electron mobility. This characteristic is preferred over a high DOS effective mass due to the limited conduction band edge degeneracy typical of half-Heuslers. In *p*-type materials, uniquely high valence band degeneracy, achievable through various positions of valence band edge extrema, emerges as the most desirable trait. Such degeneracy, when combined with steep valence band edges where possible, is also favored over simple DOS effective mass trends. For both carrier types, we seek materials with lower lattice thermal conductivity (κ_L) to further maximize the thermoelectric quality factor, β .

Using these insights, we statistically identify promising elemental subspaces. Our analysis highlights A-elements Y and Zr as well as B-element Ir for *n*-type thermoelectric materials as a result of high electron mobility. Both *n*- and *p*-type performance in Y, as well as secondary subspace based on B-element Au, are driven by low lattice thermal conductivity. B-element Ir is notable for its subset of exceptionally high TE quality factors, driven by ultra-high valence band degeneracy in *p*-type. The design rules provided by this subspace approach led to the synthesis of Sc_{0.5}Lu_{0.5}AuSn, a compound with uniquely low lattice thermal conductivity attributed to the presence of Lu and Au. Our findings offer valuable insights for the continued exploration of half-

Heusler compounds. The subspace approach combines insights from proven high-performance compounds with opportunities to explore new chemistries, identifying drivers of TE performance and guiding element-specific optimization of half-Heusler transport properties.

Conflicts of interest

There are no conflicts to declare.

Acknowledgements

All authors acknowledge support from NSF Harnessing the Data Revolution program under Grant No. 2118201. AP and EE acknowledge support from the NSF DIGI-MAT program, Grant No. 1922758. Computational resources were provided by the Advanced Cyberinfrastructure Coordination Ecosystem: Services Support (ACCESS) program through Bridges-2 at the Pittsburgh Supercomputing Center, allocation TG-MAT220011P.

Notes and references

- 1 T. Graf, C. Felser and S. S. Parkin, *Progress in solid state chemistry*, 2011, **39**, 1–50.
- 2 W. Y. S. Lim, D. Zhang, S. S. F. Duran, X. Y. Tan, C. K. I. Tan, J. Xu and A. Suwardi, *Frontiers in Materials*, 2021, **8**, 745698.
- 3 R. Nesper, *Zeitschrift für anorganische und allgemeine Chemie*, 2014, **640**, 2639–2648.
- 4 G. Bergerhoff, R. Hundt, R. Sievers and I. Brown, *Journal of chemical information and computer sciences*, 1983, **23**, 66–69.
- 5 R. Gautier, X. Zhang, L. Hu, L. Yu, Y. Lin, T. O. Sunde, D. Chon, K. R. Poepelmeier and A. Zunger, *Nature chemistry*, 2015, **7**, 308–316.
- 6 K. Ciesielski, I. Wolanska, K. Synoradzki, D. Szymanski and D. Kaczorowski, *Physical Review Applied*, 2021, **15**, 044047.
- 7 K. Ciesielski, K. Synoradzki, I. Wolanska, P. Stachowiak, L. Kepinski, A. Jezowski, T. Tolinski and D. Kaczorowski, *Journal of Alloys and Compounds*, 2020, **816**, 152596.
- 8 J. Carrete, N. Mingo, S. Wang and S. Curtarolo, *Advanced Functional Materials*, 2014, **24**, 7427–7432.
- 9 S. Chadov, X. Qi, J. Kübler, G. H. Fecher, C. Felser and S. C. Zhang, *Nature materials*, 2010, **9**, 541–545.
- 10 H. Lin, L. A. Wray, Y. Xia, S. Xu, S. Jia, R. J. Cava, A. Bansil and M. Z. Hasan, *Nature materials*, 2010, **9**, 546–549.
- 11 R. Chasmar and R. Stratton, *International journal of electronics*, 1959, **7**, 52–72.
- 12 F. A. Bipasha, L. C. Gomes, J. Qu and E. Ertekin, *Frontiers in Electronic Materials*, 2022, **2**, 1059684.
- 13 G. J. Snyder and E. S. Toberer, *Nature materials*, 2008, **7**, 105–114.
- 14 J. Qu, V. Stevanović, E. Ertekin and P. Gorai, *Journal of Materials Chemistry A*, 2020, **8**, 25306–25315.
- 15 P. Gorai, V. Stevanović and E. S. Toberer, *Nature Reviews Materials*, 2017, **2**, 1–16.
- 16 W. Chen, J.-H. Pöhls, G. Hautier, D. Broberg, S. Bajaj, U. Aydemir, Z. M. Gibbs, H. Zhu, M. Asta, G. J. Snyder *et al.*, *Journal of Materials Chemistry C*, 2016, **4**, 4414–4426.

- 17 P. Gorai, P. Parilla, E. S. Toberer and V. Stevanovic, *Chemistry of Materials*, 2015, **27**, 6213–6221.
- 18 G. K. Madsen, *Journal of the American Chemical Society*, 2006, **128**, 12140–12146.
- 19 S. A. Miller, P. Gorai, B. R. Ortiz, A. Goyal, D. Gao, S. A. Barnett, T. O. Mason, G. J. Snyder, Q. Lv, V. Stevanović *et al.*, *Chemistry of Materials*, 2017, **29**, 2494–2501.
- 20 J. Yan, P. Gorai, B. Ortiz, S. Miller, S. A. Barnett, T. Mason, V. Stevanović and E. S. Toberer, *Energy & Environmental Science*, 2015, **8**, 983–994.
- 21 G. K. Madsen and D. J. Singh, *Computer Physics Communications*, 2006, **175**, 67–71.
- 22 A. M. Ganose, J. Park, A. Faghaninia, R. Woods-Robinson, K. A. Persson and A. Jain, *Nature communications*, 2021, **12**, 2222.
- 23 J. Qu, C. E. Porter, L. C. Gomes, J. M. Adamczyk, M. Y. Toriyama, B. R. Ortiz, E. S. Toberer and E. Ertekin, *Journal of Materials Chemistry A*, 2021, **9**, 26189–26201.
- 24 S. Bhattacharya and G. K. Madsen, *Physical Review B*, 2015, **92**, 085205.
- 25 T. Jia, Z. Feng, S. Guo, X. Zhang and Y. Zhang, *ACS applied materials & interfaces*, 2020, **12**, 11852–11864.
- 26 A. D. Becke and E. R. Johnson, *The Journal of chemical physics*, 2006, **124**, year.
- 27 S. Wang, Z. Wang, W. Setyawan, N. Mingo and S. Curtarolo, *Physical Review X*, 2011, **1**, 021012.
- 28 L. Xi, S. Pan, X. Li, Y. Xu, J. Ni, X. Sun, J. Yang, J. Luo, J. Xi, W. Zhu *et al.*, *Journal of the American Chemical Society*, 2018, **140**, 10785–10793.
- 29 G. Joshi, X. Yan, H. Wang, W. Liu, G. Chen and Z. Ren, *Advanced Energy Materials*, 2011, **1**, 643–647.
- 30 S. Li, H. Zhu, J. Mao, Z. Feng, X. Li, C. Chen, F. Cao, X. Liu, D. J. Singh, Z. Ren *et al.*, *ACS applied materials & interfaces*, 2019, **11**, 41321–41329.
- 31 P. Luo, C. Lin, Z. Li, J. Zhang and J. Luo, *ACS Applied Energy Materials*, 2023, **6**, 10070–10077.
- 32 G. Rogl, P. Sauerschnig, Z. Rykavets, V. Romaka, P. Heinrich, B. Hinterleitner, A. Grytsiv, E. Bauer and P. Rogl, *Acta Materialia*, 2017, **131**, 336–348.
- 33 H. Zhu, R. He, J. Mao, Q. Zhu, C. Li, J. Sun, W. Ren, Y. Wang, Z. Liu, Z. Tang *et al.*, *Nature Communications*, 2018, **9**, 2497.
- 34 A. Sagar, A. Bhardwaj, M. Lamba, A. Novitskii, V. Khovaylo and S. Patnaik, *Bulletin of Materials Science*, 2024, **47**, 146.
- 35 W. G. Zeier, J. Schmitt, G. Hautier, U. Aydemir, Z. M. Gibbs, C. Felser and G. J. Snyder, *Nature Reviews Materials*, 2016, **1**, 1–10.
- 36 G. Kresse and J. Furthmüller, *Physical review B*, 1996, **54**, 11169.
- 37 P. E. Blöchl, *Physical review B*, 1994, **50**, 17953.
- 38 J. P. Perdew, K. Burke and M. Ernzerhof, *Physical review letters*, 1996, **77**, 3865.
- 39 F. Birch, *Elastic Properties and Equations of State*, 1988, **26**, 31–90.
- 40 S. P. Ong, W. D. Richards, A. Jain, G. Hautier, M. Kocher, S. Cholia, D. Gunter, V. L. Chevrier, K. A. Persson and G. Ceder, *Computational Materials Science*, 2013, **68**, 314–319.
- 41 K. A. Borup, E. S. Toberer, L. D. Zoltan, G. Nakatsukasa, M. Errico, J.-P. Fleurial, B. B. Iversen and G. J. Snyder, *Review of Scientific Instruments*, 2012, **83**, year.
- 42 S. Iwanaga, E. S. Toberer, A. LaLonde and G. J. Snyder, *Review of Scientific Instruments*, 2011, **82**, year.
- 43 H.-S. Kim, Z. M. Gibbs, Y. Tang, H. Wang and G. J. Snyder, *APL materials*, 2015, **3**, year.
- 44 S. Guo, S. Anand, M. K. Brod, Y. Zhang and G. J. Snyder, *Journal of Materials Chemistry A*, 2022, **10**, 3051–3057.
- 45 W. Xie, A. Weidenkaff, X. Tang, Q. Zhang, J. Poon and T. M. Tritt, *Nanomaterials*, 2012, **2**, 379–412.
- 46 X. Yan, G. Joshi, W. Liu, Y. Lan, H. Wang, S. Lee, J. Simonson, S. Poon, T. Tritt, G. Chen *et al.*, *Nano letters*, 2011, **11**, 556–560.
- 47 S. Sakurada and N. Shutoh, *Applied Physics Letters*, 2005, **86**, year.
- 48 M. T. Dylla, A. Dunn, S. Anand, A. Jain and G. J. Snyder, *Research*, 2020.
- 49 G. Li, K. Kurosaki, Y. Ohishi, H. Muta and S. Yamanaka, *Japanese Journal of Applied Physics*, 2013, **52**, 041804.
- 50 J. Oestreich, U. Probst, F. Richardt and E. Bucher, *Journal of Physics: Condensed Matter*, 2003, **15**, 635.
- 51 S. Ouardi, G. H. Fecher, C. Felser, J. Hamrle, K. Postava and J. Pištora, *Applied Physics Letters*, 2011, **99**, year.
- 52 S. Li, H. Zhao, D. Li, S. Jin and L. Gu, *Journal of Applied Physics*, 2015, **117**, year.
- 53 H. Hohl, A. Ramirez, W. Kaefer, K. Fess, C. Thurner, C. Kloc and E. Bucher, *MRS Online Proceedings Library (OPL)*, 1997, **478**, 109.
- 54 D. Young, P. Khalifah, R. J. Cava and A. Ramirez, *Journal of Applied Physics*, 2000, **87**, 317–321.
- 55 C. Shekhar, S. Ouardi, A. K. Nayak, G. H. Fecher, W. Schnelle and C. Felser, *Physical Review B*, 2012, **86**, 155314.
- 56 H. Xie, H. Wang, C. Fu, Y. Liu, G. J. Snyder, X. Zhao and T. Zhu, *Scientific reports*, 2014, **4**, 6888.
- 57 H.-H. Xie, J.-L. Mi, L.-P. Hu, N. Lock, M. Chirstensen, C.-G. Fu, B. B. Iversen, X.-B. Zhao and T.-J. Zhu, *CrystEngComm*, 2012, **14**, 4467–4471.
- 58 D. Gnida, K. Ciesielski and D. Kaczorowski, *Physical Review B*, 2021, **103**, 174206.
- 59 M. J. Winiarski and K. Bilińska, *Intermetallics*, 2019, **108**, 55–60.
- 60 C. P. Sebastian, H. Eckert, S. Rayaprol, R.-D. Hoffmann and R. Pöttgen, *Solid state sciences*, 2006, **8**, 560–566.
- 61 W. Li, S. Ghosh, N. Liu and B. Poudel, *Joule*, 2024.
- 62 K. Xia, C. Hu, C. Fu, X. Zhao and T. Zhu, *Applied Physics Letters*, 2021, **118**, year.
- 63 A. A. Shawon, W. Guetari, K. Ciesielski, R. Orenstein, J. Qu, S. Chanakian, M. T. Rahman, E. Ertekin, E. Toberer and A. Zevalkink, *Chemistry of Materials*, 2024.
- 64 K. Ciesielski, K. Synoradzki, I. Veremchuk, P. Skokowski, D. Szymański, Y. Grin and D. Kaczorowski, *Physical Review*

Electronic Supplementary Information

Angela Pak,^a Kamil Ciesielski,^b Maria Wroblewska^b, Eric S. Toberer^b, and Elif Ertekin^a

January 20, 2025

^a *University of Illinois at Urbana-Champaign, Urbana, IL 61801, USA; E-mail: ertekin@illinois.edu* ^b *Colorado School of Mines, Golden, CO 80401, USA.*

1 Band Structure Comparisons.

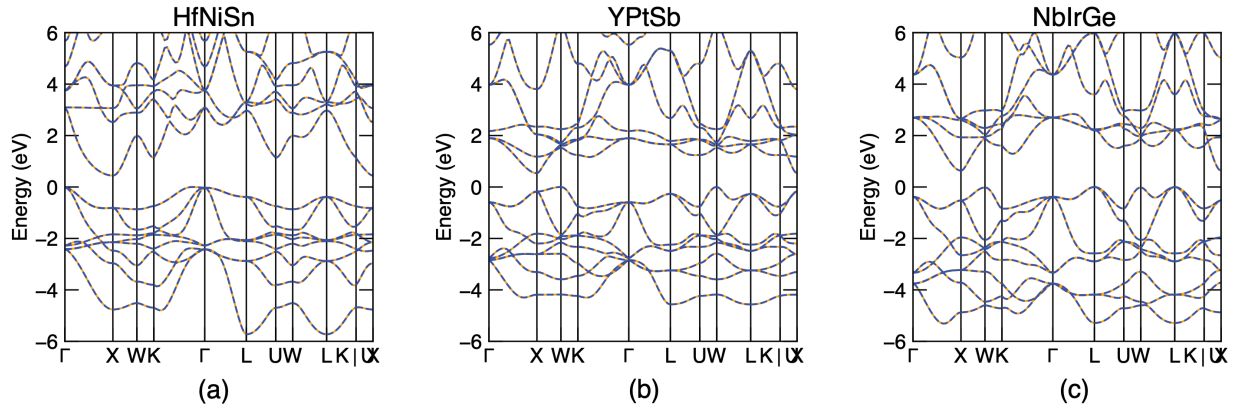


Figure 1: Calculated band structures for a) HfNiSn, a typical half-Heusler with conventional band structure features b) YPtSb, a half-Heusler predicted stable in this work with uniquely high electron mobility as anticipated by the steeper conduction band (CB) edge but still with a CB edge degeneracy of 3 at X -point and c) NbIrGe, a half-Heusler with uniquely high degeneracy at the valence band edge as seen by W , Γ , and X -points all reaching similar energy eigenvalues.

2 Correlations.

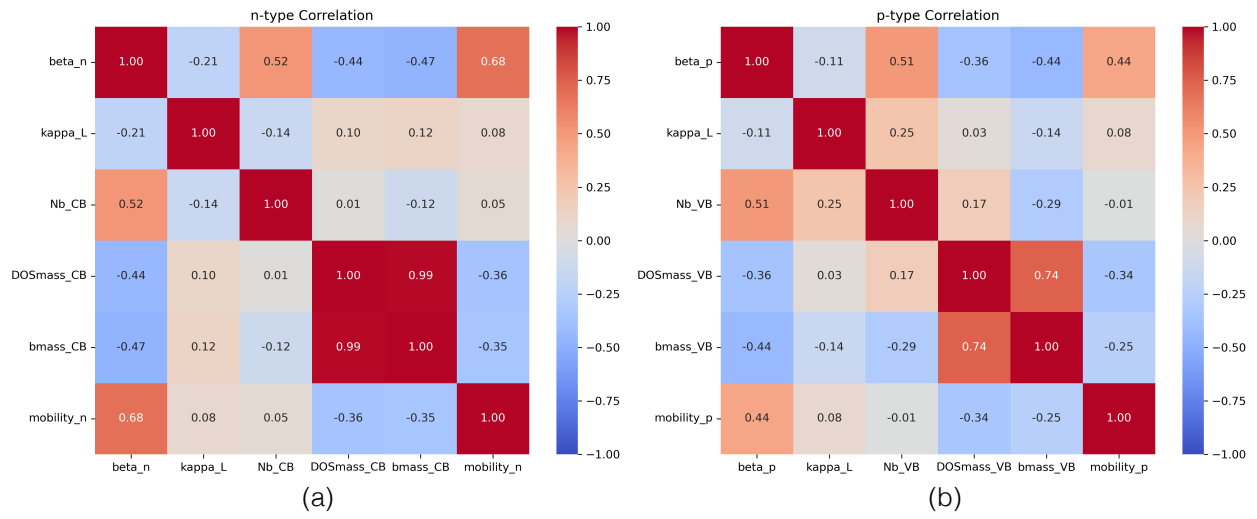


Figure 2: Pearson correlation coefficients of TE quality factor β and each of its components for n - and p -type data.

3 Group Number Comparisons.

As chemistry-specific trends were pursued to offer design rules in high-performing thermoelectrics, their performance alongside other descriptors were evaluated to ensure that chosen subspaces maintained high β . A common descriptor with which to analyze half-Heuslers is the group number difference between each of their ABC elements respectively. This is particularly useful in the case of our work as it is focused on 18-electron systems, so the chemistries considered fall into a rather limited range of group number differences. The highest-performing half-Heuslers were found to spread across nearly the entirety of possible group number differences. This indicates that a selection of subspace by group number would not have captured the desirable transport trends evaluated in this work to the extent that chemistry-based subspaces did. Additionally, the highest β_n overall for each pair-wise group number comparison was often found in a compound that belonged to a high-performing subspace. The same is true for β_p as well.

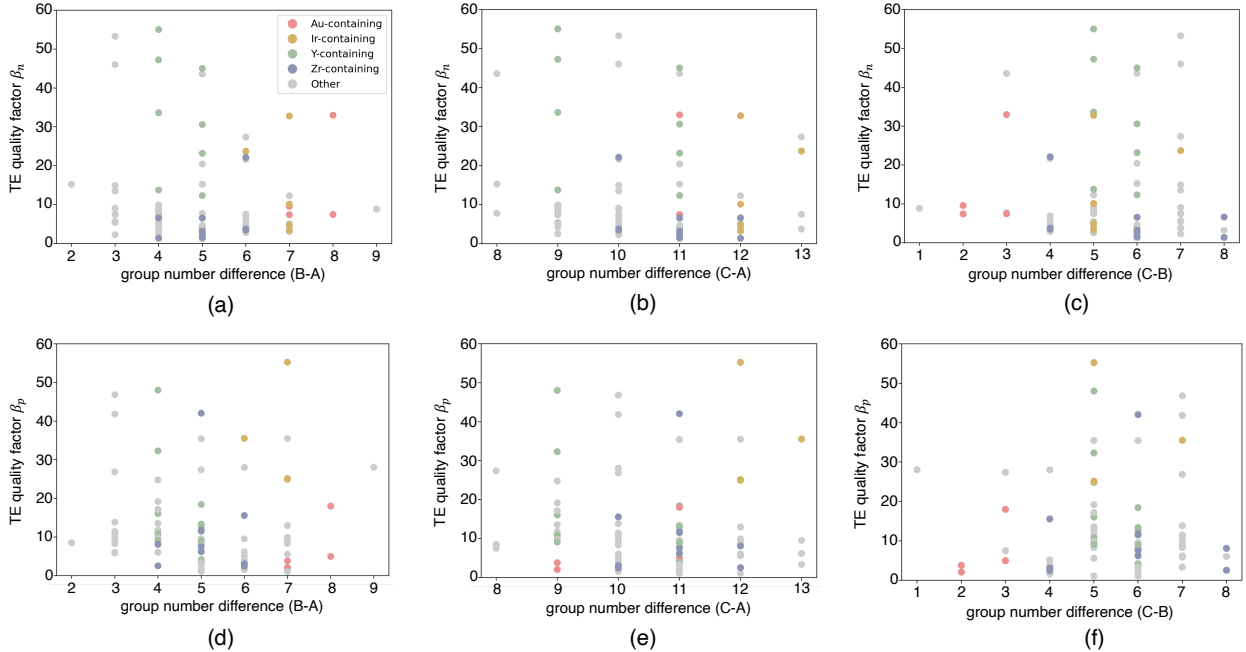


Figure 3: β values for n-type performance (a), (b), and (c) as well as for p-type performance (d), (e), and (f), visualized by difference in group numbers between ABC element pairs. Chemistries are colored accordingly if they belonged to a subspace named in this work.

4 Additional Semiconductor Data - Transport.

Table 1: Electronic Transport, n-type

Compound	$m_{DOS}(m_e)$	N_b	$m_b(m_e)$	$\mu_n(\frac{cm^2}{Vs})$	$\kappa(\frac{W}{mK})$
AcNiAs	0.076	3	0.036	1321.419	5.876
AcNiP	2.717	3	1.306	6.633	7.25
AcNiSb	2.387	3	1.148	6.814	5.157
CoMoAl	1.961	9	0.453	55.478	22.953
CrCoAl	2.859	3	1.374	12.112	31.889
CrCoB	0.765	3	0.368	129.21	51.699
CrCoGa	1.706	3	0.82	27.171	24.873
CrCoIn	6.682	6	2.024	5.809	17.093
CrFeC	2.153	3	1.035	30.82	61.675
CrFeGe	2.168	3	1.042	21.423	31.988
CrFeSi	4.218	3	2.028	8.628	48.319
CrFeSn	1.269	3	0.61	39.375	21.467
CrIrAl	3.658	3	1.759	9.217	23.511
CrIrB	4.395	3	2.113	9.271	31.7
CrIrGa	2.505	3	1.204	16.617	21.008
CrIrIn	4.329	3	2.081	6.184	16.043
CrIrTl	2.464	3	1.185	36.501	97.764
CrOsGe	4.827	3	2.321	6.872	25.716
CrOsPb	4.195	3	2.017	6.289	12.579
CrOsSi	7.374	3	3.545	3.923	32.723
CrOsSn	4.933	3	2.372	5.726	20.175
CrReAs	4.709	3	2.264	6.973	25.314
CrReP	3.635	3	1.748	11.373	32.444
CrReSb	6.269	3	3.014	3.995	20.774
CrRhAl	5.215	3	2.507	4.821	28.548
CrRhB	1.995	3	0.959	27.765	41.078
CrRhGa	4.461	3	2.144	6.234	23.483
CrRuC	4.221	3	2.029	10.023	47.53
CrRuGe	3.751	3	1.803	9.217	30.488
CrRuPb	4.043	3	1.944	6.279	13.891
CrRuSi	5.917	3	2.845	5.017	42.159
CrRuSn	4.042	3	1.943	7.065	22.551
CrTcAs	3.799	3	1.826	9.104	31.938
CrTcP	5.317	3	2.556	6.049	43.702
CrTcSb	3.465	3	1.666	9.094	24.251
FeMoSi	6.254	3	3.007	4.057	33.98
HfAgAl	0.795	3	0.382	53.927	10.457
HfAgB	1.119	3	0.538	41.258	13.008
HfAgGa	0.906	3	0.435	44.841	9.005
HfAuAl	1.188	3	0.571	35.27	11.248
HfAuB	1.574	3	0.757	27.838	12.876
HfAuGa	1.266	3	0.608	32.074	9.886
HfAuIn	1.125	3	0.541	34.872	8.702
HfAuTl	1.039	3	0.499	36.495	6.512
HfCoAs	4.295	3	2.065	6.52	16.463
HfCoBi	3.523	3	1.694	6.826	9.148
HfCoP	3.888	3	1.869	8.292	20.825
HfCoSb	3.188	3	1.533	9.086	13.888
HfCuB	0.943	3	0.453	61.423	15.441
HfFeTe	0.742	3	0.357	82.067	14
HfIrSb	0.282	3	0.136	381.509	14.884

HfNiC	2.696	3	1.296	14.986	18.405
HfNiGe	1.817	3	0.874	21.485	14.278
HfNiSi	1.762	3	0.847	24.24	18.593
HfNiSn	1.592	3	0.765	23.172	11.798
HfPdSn	1.464	3	0.704	25.639	11.835
HfPtGe	2.541	3	1.221	13.727	13.747
HfPtPb	1.914	3	0.92	17.359	8.779
HfPtSi	2.379	3	1.144	16.227	16.772
HfPtSn	1.902	3	0.914	19.731	12.551
HfRhAs	0.257	3	0.124	427.148	16.498
HfRhBi	0.238	3	0.114	399.445	10.308
HfRhP	0.616	3	0.296	124.674	20.229
HfRhSb	3.26	3	1.567	8.907	15.157
HfRuTe	0.207	9	0.048	1693.412	15.359
LaAuSi	1.331	6	0.403	35.932	6.657
LaAuSn	1.28	6	0.388	34.087	4.964
LaCoS	0.604	9	0.14	227.013	11.445
LaCoSe	0.248	9	0.057	792.901	8.946
LaCoTe	4.619	9	1.068	9.137	7.761
LaCuC	1.852	3	0.89	12.665	9.033
LaFeF	13.1	9	3.028	0.801	2.357
LaHgAl	1.07	9	0.247	55.481	4.438
LaHgIn	1	3	0.481	18.794	3.311
LaNiAs	2.906	9	0.672	18.786	8.716
LaNiP	3.062	9	0.708	18.906	11.431
LaNiSb	2.491	9	0.576	21.568	7.328
LaPtSb	0.056	9	0.013	6903.559	6.935
LaRhS	0.2	9	0.046	1162.399	11.125
LaRhSe	0.151	9	0.035	1659.377	9.172
LaRhTe	2.653	9	0.613	21.554	8.343
LaRuF	3.016	9	0.697	17.112	6.573
MnNiB	19.488	3	9.369	0.81	34.551
MoIrB	1.567	3	0.753	44.496	34.243
MoIrTl	1.76	3	0.846	25.461	14.783
MoOsPb	2.861	3	1.375	12.925	16.684
MoRhB	1.143	3	0.55	66.078	41.263
NbCoC	5.046	3	2.426	7.541	45.876
NbCoGe	3.725	6	1.128	18.082	28.371
NbCoPb	3.292	3	1.582	8.505	13.353
NbCoSi	1.942	3	0.934	25.698	39.32
NbCoSn	3.463	9	0.8	26.213	21.288
NbFeAs	0.733	3	0.352	108.219	30.924
NbFeBi	1.133	3	0.544	43.533	14.71
NbFeP	0.662	3	0.318	139.896	43.627
NbFeSb	0.931	3	0.448	66.827	24.157
NbIrC	0.226	3	0.109	727.35	28.682
NbIrGe	0.366	3	0.176	310.733	24.695
NbIrPb	0.93	3	0.447	63.195	14.604
NbIrSi	0.608	3	0.292	155.315	30.969
NbIrSn	0.785	3	0.377	90.355	21.168
NbNiAl	0.416	3	0.2	201.235	26.615
NbNiB	2.127	3	1.023	24.087	39.501
NbNiTl	2.587	3	1.244	11.319	11.483
NbOsAs	0.733	3	0.352	112.42	25.856
NbOsBi	0.912	3	0.438	67.354	16.047
NbOsP	0.553	3	0.266	185.802	32.018
NbOsSb	0.706	3	0.34	111.517	23.51

NbPtAl	0.487	3	0.234	175.48	22.028
NbPtB	0.741	3	0.356	115.026	27.043
NbPtGa	0.453	3	0.218	198.484	19.438
NbPtIn	0.647	3	0.311	103.858	16.101
NbPtTl	4.902	3	2.357	4.722	12.012
NbRhC	2.354	3	1.131	21.15	38.361
NbRhGe	0.677	3	0.326	113.678	27.798
NbRhPb	1.246	3	0.599	36.865	14.454
NbRhSi	0.662	3	0.318	125.215	36.656
NbRhSn	0.929	3	0.446	63.614	22.356
NbRuAs	0.659	3	0.317	124.545	30.583
NbRuBi	0.967	3	0.465	57.232	16.689
NbRuP	0.634	3	0.305	143.345	40.237
NbRuSb	0.768	3	0.369	91.293	25.982
ScAgC	2.384	3	1.146	10.417	13.918
ScAuGe	1.838	3	0.884	14.266	8.983
ScAuSi	1.815	3	0.872	16.161	12.259
ScAuSn	1.596	3	0.767	16.46	7.998
ScCdIn	2.127	3	1.023	6.778	5.12
ScCdTl	2.125	3	1.022	6.047	3.198
ScCoS	1	3	0.481	47.661	23.676
ScCoSe	0.411	3	0.197	165.818	16.688
ScCoTe	4.093	3	1.967	4.919	13.946
ScCuC	1.828	3	0.879	19.205	21.654
ScHgAl	1.155	3	0.555	22.261	7.324
ScHgB	1.625	3	0.781	16.472	8.589
ScHgGa	1.339	3	0.644	16.976	5.606
ScHgIn	1.301	3	0.626	16.335	4.911
ScHgTl	1.384	3	0.666	12.814	3.12
ScNiAs	2.667	3	1.282	9.834	17.218
ScNiBi	2.308	3	1.11	9.315	7.512
ScNiP	2.997	3	1.441	9.201	26.032
ScNiSb	2.222	3	1.068	11.478	13.143
ScPtP	0.119	3	0.057	1146.887	15.557
ScPtSb	2.984	3	1.434	8.11	11.6
ScRhTe	0.987	3	0.474	41.671	14.184
TaCoC	4.935	3	2.372	7.878	27.988
TaCoGe	3.19	3	1.533	12.12	21.702
TaCoPb	3.059	3	1.471	10.089	11.659
TaCoSi	3.444	3	1.656	11.588	27.858
TaCoSn	2.854	3	1.372	12.459	17.37
TaFeAs	0.827	3	0.397	94.991	23.159
TaFeBi	3.754	3	1.805	7.636	12.74
TaFeP	0.711	3	0.342	132.24	30.139
TaFeSb	1.036	9	0.239	182.019	19.694
TaIrGe	0.7	3	0.337	124.639	21.433
TaIrSi	0.629	3	0.302	155.655	25.763
TaIrSn	0.831	9	0.192	264.631	18.999
TaNiAl	1.341	3	0.645	37.487	19.322
TaNiB	1.764	3	0.848	33.493	26.023
TaNiGa	1.54	3	0.74	31.667	17.265
TaNiIn	1.574	3	0.757	26.423	13.59
TaNiTl	1.511	3	0.726	26.885	9.943
TaOsBi	2.411	3	1.159	16.368	14.417
TaOsP	0.183	3	0.088	1005.257	25.608
TaOsSb	0.724	3	0.348	113.447	20.732
TaPtAl	0.647	3	0.311	123.767	19.148

TaPtB	1.08	3	0.519	69.073	22.289
TaPtGa	0.895	3	0.43	77.138	17.454
TaPtIn	2.308	3	1.11	16.615	14.747
TaPtTl	3.518	3	1.691	8.342	11.369
TaRhC	0.32	3	0.154	425.167	25.588
TaRhGe	0.853	3	0.41	85.417	22.374
TaRhPb	2.86	3	1.375	11.292	12.957
TaRhSi	0.64	3	0.308	139.215	27.616
TaRhSn	1.354	3	0.651	38.52	18.934
TaRuAs	0.457	3	0.22	225.25	23.838
TaRuBi	0.365	3	0.175	260.342	14.695
TaRuP	0.647	3	0.311	144.094	29.147
TaRuSb	0.743	3	0.357	101.495	21.745
TiAgAl	1.323	3	0.636	23.199	14.475
TiAgB	2.208	3	1.062	14.625	20.379
TiAgGa	1.625	3	0.781	17.157	11.304
TiAgIn	1.929	3	0.927	11.668	8.723
TiAuAl	3.163	3	1.521	7.681	13.674
TiAuB	3.85	3	1.851	7.358	17.467
TiAuGa	3.196	3	1.537	7.535	11.444
TiAuIn	2.925	3	1.406	7.593	9.318
TiAuTl	2.888	3	1.389	7.046	6.414
TiCoAs	6.119	3	2.942	3.909	27.012
TiCoBi	5.518	3	2.653	3.439	11.586
TiCoP	5.408	3	2.6	5.305	41.292
TiCoSb	5.346	3	2.57	4.167	20.007
TiCuB	1.508	3	0.725	31.047	30.147
TiCuGa	1.098	3	0.528	35.651	14.812
TiFePo	0.952	3	0.458	48.752	12.179
TiFeS	1.777	3	0.854	26.948	37.198
TiFeSe	1.23	3	0.591	42.092	25.25
TiFeTe	1.952	3	0.939	19.394	20.72
TiIrAs	0.984	9	0.227	189.135	20.877
TiIrBi	2.723	3	1.309	11.076	12.211
TiIrP	1.344	3	0.646	43.503	26.911
TiIrSb	3.139	3	1.509	10.327	18.847
TiNiC	3.714	3	1.786	10.253	42.616
TiNiGe	2.661	3	1.279	12.185	22.947
TiNiPb	2.95	3	1.418	7.873	9.439
TiNiSi	2.49	3	1.197	14.6	34.866
TiNiSn	2.688	3	1.292	10.23	16.271
TiOsTe	0.27	3	0.13	415.51	19.158
TiPtC	0.225	3	0.108	611.196	21.407
TiPtGe	4.282	3	2.058	6.274	17.623
TiPtPb	8.32	3	4	1.819	9.516
TiPtSi	1.559	3	0.75	31.021	23.056
TiPtSn	7.17	3	3.447	2.607	14.813
TiRhAs	1.86	3	0.894	22.306	24.728
TiRhBi	7.145	3	3.435	2.355	12.402
TiRhP	1.585	3	0.762	31.349	34.664
TiRhSb	4.431	3	2.13	5.536	20.385
TiRuTe	2.81	3	1.351	11.325	21.373
VCoC	1.278	3	0.615	62.521	54.667
VCoGe	1.898	3	0.913	24.372	28.749
VCoPb	5.496	3	2.642	3.659	11.589
VCoSi	1.331	3	0.64	45.403	43.617
VCoSn	3.531	3	1.697	8.095	20.19

VFeAs	1.493	3	0.718	37.493	33.002
VFeBi	4.83	3	2.322	4.697	13.387
VFeP	1.088	3	0.523	68.179	50.492
VFeSb	1.705	9	0.394	78.98	23.948
VIrC	2.387	3	1.148	22.358	29.679
VIrGe	1.271	3	0.611	47.462	23.481
VIrSi	0.995	3	0.478	74.254	30.364
VIrSn	1.547	3	0.744	31.143	19.14
VNiAl	6.03	3	2.899	3.489	27.727
VNiB	4.588	3	2.206	7.666	43.682
VNiGa	4.611	3	2.217	5.411	21.417
VNiIn	8.035	3	3.863	1.956	14.656
VOsAs	1.209	3	0.581	53.809	25.884
VOsBi	3.802	3	1.828	7.531	14.302
VOsP	0.984	3	0.473	80.583	32.945
VOsSb	1.788	3	0.86	26.834	21.861
VPtAl	1.141	3	0.548	46.467	19.725
VPtB	1.221	3	0.587	54.953	26.006
VPtGa	1.835	3	0.882	23.034	17.137
VPtTl	10.568	3	5.08	1.332	9.599
VReTe	1.92	3	0.923	23.038	20.366
VRhC	1.26	3	0.606	55.722	41.134
VRhGe	1.367	6	0.414	76.818	26.799
VRhPb	7.717	3	3.71	2.226	12.653
VRhSi	1.133	3	0.545	55.437	38.003
VRhSn	2.099	3	1.009	17.689	20.572
VRuAs	1.297	3	0.624	45.022	31.356
VRuBi	3.691	3	1.775	7.278	15.129
VRuP	1.034	3	0.497	69.881	43.453
VRuSb	1.482	3	0.712	32.719	24.605
VTcTe	1.23	3	0.592	41.725	23.452
WCoAl	0.584	3	0.281	157.497	25.067
WCoB	0.415	3	0.199	353.811	34.205
WCoGa	0.554	3	0.266	176.202	22.46
WCoIn	2.412	9	0.558	49.424	17.223
WFeC	0.497	3	0.239	280.748	34.998
WFeGe	0.417	3	0.201	291.356	26.57
WFeSi	0.298	3	0.143	521.644	34.286
WFeSn	0.602	3	0.289	145.838	21.081
WIrAl	1.393	3	0.67	46.587	24.788
WIrB	0.342	3	0.164	463.913	29.443
WIrGa	1.057	3	0.508	71.557	22.785
WIrIn	0.521	3	0.251	183.891	19.291
WIrTl	0.819	3	0.394	87.779	14.692
WOsGe	1.606	3	0.772	0.77	0.188
WOsPb	0.58	3	0.279	152.608	16.166
WOsSn	1.434	3	0.689	43.498	22.495
WRhAl	1.762	3	0.847	29.48	25.705
WRhB	0.28	3	0.135	582.309	32.079
WRhGa	0.644	3	0.31	136.165	22.988
WRhIn	0.763	3	0.367	93.28	18.786
WRhTl	0.929	3	0.446	65.967	13.97
WRuPb	0.578	3	0.278	142.292	16.132
YAgC	0.862	3	0.414	39.584	9.571
YAgSi	1.265	3	0.608	20.419	10.09
YAuGe	0.655	6	0.198	113.613	6.864
YAuSi	1.525	6	0.462	34.961	8.958

YAuSn	1.082	6	0.328	51.097	6.347
YCoS	0.303	3	0.146	235.286	14.88
YCoTe	4.193	3	2.016	4.039	10.156
YCuC	1.403	3	0.674	22.965	13.348
YCuGe	1.327	3	0.638	19.454	8.906
YCuSi	1.173	3	0.564	25.146	12.422
YHgAl	0.926	6	0.28	54.494	5.878
YHgB	1.374	3	0.66	17.45	6.348
YNiAs	2.58	3	1.24	8.653	11.81
YNiBi	2.033	3	0.977	9.807	5.961
YNiP	2.557	3	1.229	9.573	16.19
YNiSb	2.102	3	1.01	10.664	9.611
YPtAs	0.663	3	0.319	67.794	9.285
YPtBi	0.774	3	0.372	46.457	6.182
YPtP	0.236	3	0.114	338.009	11.022
YPtSb	0.064	3	0.031	2203.969	8.753
YRhTe	0.332	3	0.159	182.777	10.473
ZrAgB	1.136	6	0.344	75.632	17.937
ZrAuAl	1.212	6	0.367	63.459	13.318
ZrAuB	1.729	6	0.524	45.178	15.809
ZrAuGa	1.362	6	0.413	53.135	11.294
ZrAuTl	1.425	3	0.685	21.3	7.128
ZrCoAs	3.977	3	1.912	6.873	22.023
ZrCoBi	3.405	3	1.637	6.802	10.823
ZrCoP	4.289	3	2.062	6.764	30.713
ZrCoSb	3.401	3	1.635	7.75	17.458
ZrCuB	0.817	6	0.247	143.089	23.408
ZrFePo	0.335	3	0.161	221.121	11.063
ZrFeS	0.468	3	0.225	178.142	27.06
ZrFeSe	0.313	3	0.151	299.739	20.319
ZrFeTe	7.255	3	3.488	2.518	17.543
ZrIrAs	0.118	3	0.057	1398.387	18.216
ZrIrBi	0.112	6	0.034	2560.732	11.814
ZrIrP	0.191	9	0.044	2190.353	22.455
ZrIrSb	4.586	6	1.389	11.057	17.285
ZrNiC	2.625	3	1.262	15.109	30.211
ZrNiGe	1.774	3	0.853	20.922	19.182
ZrNiPb	1.698	9	0.393	53.479	9.374
ZrNiSi	1.942	3	0.934	19.491	26.606
ZrNiSn	1.781	3	0.856	18.318	14.748
ZrPtPb	2.039	3	0.98	14.95	9.775
ZrPtSi	2.737	6	0.829	24.653	20.274
ZrPtSn	2.059	3	0.99	16.519	14.412
ZrRhAs	3.305	3	1.589	8.892	21.726
ZrRhBi	4.045	6	1.225	10.915	12.261
ZrRhP	4.439	6	1.344	12.348	28.405
ZrRhSb	3.712	3	1.785	6.933	18.575
ZrRuTe	0.728	3	0.35	81.82	19.157

Table 2: Electronic Transport, p-type

Compound	$m_{DOS}(m_e)$	N_b	$m_b(m_e)$	$\mu_p(\frac{cm^2}{Vs})$	$\kappa(\frac{W}{mK})$
AcNiAs	9.703	14	1.67	4.236	5.876
AcNiP	9.032	8	2.258	2.918	7.25
AcNiSb	1.684	14	0.29	53.657	5.157
CoMoAl	1.08	14	0.186	211.221	22.953

CrCoAl	2.786	14	0.48	58.757	31.889
CrCoB	3.145	8	0.786	41.312	51.699
CrCoGa	2.492	14	0.429	71.815	24.873
CrCoIn	2.853	14	0.491	48.575	17.093
CrFeC	4.379	8	1.095	28.327	61.675
CrFeGe	9.713	8	2.428	6.026	31.988
CrFeSi	6.914	8	1.729	10.964	48.319
CrFeSn	9.504	14	1.636	8.967	21.467
CrIrAl	4.885	14	0.841	27.872	23.511
CrIrB	3.366	8	0.841	36.896	31.7
CrIrGa	4.707	14	0.81	30.109	21.008
CrIrIn	4.323	14	0.744	28.927	16.043
CrIrTl	2.488	17	0.376	203.945	97.764
CrOsGe	4.815	8	1.204	18.398	25.716
CrOsPb	5.266	14	0.907	20.864	12.579
CrOsSi	4.83	8	1.207	19.737	32.723
CrOsSn	4.83	14	0.832	27.579	20.175
CrReAs	5.28	8	1.32	15.663	25.314
CrReP	4.878	8	1.219	19.511	32.444
CrReSb	4.122	8	1.03	19.979	20.774
CrRhAl	6.964	14	1.199	14.577	28.548
CrRhB	1.911	8	0.478	78.964	41.078
CrRhGa	4.352	14	0.749	30.187	23.483
CrRuC	3.567	8	0.892	34.408	47.53
CrRuGe	4.299	14	0.74	35.058	30.488
CrRuPb	3.934	14	0.677	30.53	13.891
CrRuSi	3.889	14	0.669	43.945	42.159
CrRuSn	3.846	14	0.662	35.524	22.551
CrTcAs	3.461	8	0.865	27.919	31.938
CrTcP	5.834	8	1.458	14.037	43.702
CrTcSb	4.227	8	1.057	17.999	24.251
FeMoSi	3.714	8	0.929	23.638	33.98
HfAgAl	6.052	3	2.909	2.569	10.457
HfAgB	2.139	3	1.028	15.615	13.008
HfAgGa	3.658	3	1.759	5.523	9.005
HfAuAl	8.699	3	4.182	1.781	11.248
HfAuB	2.319	3	1.115	15.557	12.876
HfAuGa	4.244	3	2.04	5.223	9.886
HfAuIn	3.379	3	1.624	6.701	8.702
HfAuTl	2.486	3	1.195	9.859	6.512
HfCoAs	8.412	8	2.103	6.344	16.463
HfCoBi	6.507	11	1.316	9.972	9.148
HfCoP	8.331	8	2.083	7.05	20.825
HfCoSb	9.607	8	2.402	4.632	13.888
HfCuB	2.575	3	1.238	13.613	15.441
HfFeTe	5.758	8	1.44	10.113	14
HfIrSb	3.024	3	1.454	10.878	14.884
HfNiC	1.449	3	0.697	38.044	18.405
HfNiGe	2.783	3	1.338	11.334	14.278
HfNiSi	4.536	3	2.181	5.868	18.593
HfNiSn	2.761	3	1.328	10.141	11.798
HfPdSn	2.186	3	1.051	14.06	11.835
HfPtGe	2.285	3	1.098	16.099	13.747
HfPtPb	2.037	3	0.979	15.807	8.779
HfPtSi	3.227	3	1.552	10.272	16.772
HfPtSn	2.443	3	1.175	13.55	12.551
HfRhAs	1.778	3	0.855	23.533	16.498

HfRhBi	1.811	3	0.871	18.968	10.308
HfRhP	1.884	3	0.906	23.287	20.229
HfRhSb	2.129	3	1.023	16.877	15.157
HfRuTe	4.851	3	2.332	4.974	15.359
LaAuSi	1.121	6	0.339	46.514	6.657
LaAuSn	1.417	14	0.244	68.231	4.964
LaCoS	10.086	10	2.173	3.697	11.445
LaCoSe	10.47	10	2.256	3.214	8.946
LaCoTe	9.49	1	9.49	0.345	7.761
LaCuC	4.779	6	1.447	6.111	9.033
LaFeF	11.622	5	3.975	0.533	2.357
LaHgAl	4.102	17	0.62	13.964	4.438
LaHgIn	4.6	17	0.696	10.792	3.311
LaNiAs	7.573	1	7.573	0.496	8.716
LaNiP	8.187	10	1.764	4.804	11.431
LaNiSb	1.674	1	1.674	4.352	7.328
LaPtSb	1.176	14	0.202	112.472	6.935
LaRhS	4.893	5	1.673	5.334	11.125
LaRhSe	4.274	2	2.692	2.459	9.172
LaRhTe	3.247	2	2.046	3.537	8.343
LaRuF	8.297	1	8.297	0.417	6.573
MnNiB	21.477	6	6.504	1.401	34.551
MoIrB	2.326	8	0.582	65.625	34.243
MoIrTl	1.31	6	0.397	79.26	14.783
MoOsPb	3.887	14	0.669	38.087	16.684
MoRhB	1.303	14	0.224	253.598	41.263
NbCoC	4.881	8	1.22	21.14	45.876
NbCoGe	7.198	14	1.239	15.705	28.371
NbCoPb	7.896	14	1.359	10.682	13.353
NbCoSi	7.016	6	2.125	7.486	39.32
NbCoSn	9.107	14	1.568	9.564	21.288
NbFeAs	4.522	8	1.131	18.827	30.924
NbFeBi	4.49	8	1.122	14.706	14.71
NbFeP	4.125	8	1.031	23.978	43.627
NbFeSb	4.652	10	1.002	19.955	24.157
NbIrC	2.772	8	0.693	45.077	28.682
NbIrGe	5.902	14	1.016	22.42	24.695
NbIrPb	5.466	14	0.941	20.693	14.604
NbIrSi	4.626	14	0.796	34.512	30.969
NbIrSn	4.541	14	0.782	30.29	21.168
NbNiAl	0.446	6	0.135	362.004	26.615
NbNiB	2.848	6	0.862	31.099	39.501
NbNiTl	1.248	9	0.289	101.285	11.483
NbOsAs	2.099	8	0.525	61.845	25.856
NbOsBi	2.562	8	0.641	38.144	16.047
NbOsP	2.14	8	0.535	65.079	32.018
NbOsSb	2.564	8	0.641	42.995	23.51
NbPtAl	2.059	6	0.624	40.375	22.028
NbPtB	2.481	6	0.751	37.532	27.043
NbPtGa	2.41	6	0.73	32.336	19.438
NbPtIn	1.538	6	0.466	56.706	16.101
NbPtTl	1.375	6	0.416	63.572	12.012
NbRhC	3.714	8	0.928	28.454	38.361
NbRhGe	2.821	6	0.854	26.74	27.798
NbRhPb	6.426	6	1.946	6.297	14.454
NbRhSi	2.086	6	0.632	44.738	36.656
NbRhSn	5.948	6	1.801	7.85	22.356

NbRuAs	2.604	8	0.651	42.265	30.583
NbRuBi	3.185	8	0.796	25.529	16.689
NbRuP	2.579	8	0.645	46.566	40.237
NbRuSb	2.952	8	0.738	32.326	25.982
ScAgC	0.956	3	0.459	41.05	13.918
ScAuGe	1.572	3	0.756	18.035	8.983
ScAuSi	1.783	3	0.857	16.592	12.259
ScAuSn	1.752	3	0.842	14.306	7.998
ScCdIn	2.674	3	1.286	4.808	5.12
ScCdTl	2.42	3	1.163	4.976	3.198
ScCoS	5.325	2	3.354	2.585	23.676
ScCoSe	4.677	3	2.249	4.312	16.688
ScCoTe	3.192	3	1.535	7.14	13.946
ScCuC	0.896	3	0.431	55.983	21.654
ScHgAl	3.62	3	1.741	4.014	7.324
ScHgB	1.802	3	0.866	14.112	8.589
ScHgGa	2.791	3	1.342	5.642	5.606
ScHgIn	2.662	3	1.28	5.583	4.911
ScHgTl	2.371	3	1.14	5.716	3.12
ScNiAs	1.418	3	0.682	25.378	17.218
ScNiBi	1.312	3	0.631	21.747	7.512
ScNiP	1.607	3	0.773	23.428	26.032
ScNiSb	1.551	3	0.746	19.676	13.143
ScPtP	1.09	2	0.687	27.739	15.557
ScPtSb	1.257	3	0.604	29.667	11.6
ScRhTe	1.18	3	0.567	31.86	14.184
TaCoC	5.02	8	1.255	20.475	27.988
TaCoGe	7.87	14	1.355	14.595	21.702
TaCoPb	9.4	17	1.422	10.612	11.659
TaCoSi	8.629	8	2.157	7.792	27.858
TaCoSn	9.229	14	1.589	9.997	17.37
TaFeAs	4.144	8	1.036	22.576	23.159
TaFeBi	4.754	8	1.188	14.288	12.74
TaFeP	4.079	8	1.02	25.664	30.139
TaFeSb	4.777	8	1.194	16.347	19.694
TaIrGe	4.481	8	1.12	20.525	21.433
TaIrSi	6.045	8	1.511	13.927	25.763
TaIrSn	6.442	8	1.611	10.906	18.999
TaNiAl	0.988	14	0.17	276.409	19.322
TaNiB	4.138	11	0.837	34.179	26.023
TaNiGa	1.29	14	0.222	192.613	17.265
TaNiIn	1.463	11	0.296	108.21	13.59
TaNiTl	2.564	3	1.233	12.164	9.943
TaOsBi	2.528	8	0.632	40.667	14.417
TaOsP	2.372	8	0.593	57.653	25.608
TaOsSb	2.516	8	0.629	46.648	20.732
TaPtAl	2.776	8	0.694	37.112	19.148
TaPtB	6.746	3	3.243	4.423	22.289
TaPtGa	4.401	11	0.89	25.941	17.454
TaPtIn	4.024	3	1.935	7.219	14.747
TaPtTl	3.945	3	1.896	7.025	11.369
TaRhC	5.181	11	1.047	23.982	25.588
TaRhGe	9.161	11	1.852	8.893	22.374
TaRhPb	6.398	3	3.076	3.375	12.957
TaRhSi	7.415	8	1.854	9.41	27.616
TaRhSn	8.942	11	1.808	8.321	18.934
TaRuAs	2.816	8	0.704	39.233	23.838

TaRuBi	3.106	8	0.777	27.956	14.695
TaRuP	2.795	8	0.699	42.766	29.147
TaRuSb	3.144	8	0.786	31.117	21.745
TiAgAl	8.202	3	3.943	1.503	14.475
TiAgB	3.813	3	1.833	6.445	20.379
TiAgGa	6.771	3	3.255	2.017	11.304
TiAgIn	6.134	3	2.949	2.057	8.723
TiAuAl	12.11	3	5.822	1.025	13.674
TiAuB	4.128	3	1.984	6.628	17.467
TiAuGa	8.274	3	3.978	1.809	11.444
TiAuIn	7.126	3	3.426	1.997	9.318
TiAuTl	6.068	3	2.917	2.314	6.414
TiCoAs	9.759	3	4.692	1.941	27.012
TiCoBi	7.742	3	3.722	2.07	11.586
TiCoP	10.337	11	2.09	7.361	41.292
TiCoSb	10.583	11	2.14	5.487	20.007
TiCuB	4.091	3	1.967	6.947	30.147
TiCuGa	6.622	3	3.183	2.406	14.812
TiFePo	7.996	11	1.617	7.34	12.179
TiFeS	7.086	8	1.772	9.027	37.198
TiFeSe	6.03	8	1.508	10.334	25.25
TiFeTe	6.729	8	1.682	8.081	20.72
TiIrAs	4.69	3	2.255	6.057	20.877
TiIrBi	4.564	3	2.194	5.104	12.211
TiIrP	4.86	3	2.337	6.329	26.911
TiIrSb	4.927	3	2.369	5.251	18.847
TiNiC	2.717	3	1.306	16.385	42.616
TiNiGe	5.285	3	2.541	4.354	22.947
TiNiPb	3.865	3	1.858	5.249	9.439
TiNiSi	7.874	3	3.785	2.597	34.866
TiNiSn	5.026	3	2.416	4.002	16.271
TiOsTe	6.4	3	3.077	3.598	19.158
TiPtC	2.395	2	1.509	11.756	21.407
TiPtGe	4.539	3	2.182	5.748	17.623
TiPtPb	4.069	3	1.956	5.317	9.516
TiPtSi	6.095	3	2.93	4.014	23.056
TiPtSn	5.232	3	2.515	4.183	14.813
TiRhAs	4.254	3	2.045	6.447	24.728
TiRhBi	4.25	3	2.043	5.134	12.402
TiRhP	3.384	3	1.627	10.053	34.664
TiRhSb	4.6	3	2.211	5.234	20.385
TiRuTe	5.747	3	2.763	3.872	21.373
VCoC	5.644	11	1.141	24.714	54.667
VCoGe	11.765	8	2.941	4.213	28.749
VCoPb	11.841	3	5.692	1.157	11.589
VCoSi	9.743	8	2.436	6.11	43.617
VCoSn	13.44	11	2.717	3.997	20.19
VFeAs	5.431	8	1.358	14.41	33.002
VFeBi	7.428	8	1.857	6.567	13.387
VFeP	4.795	8	1.199	19.654	50.492
VFeSb	6.419	8	1.605	9.608	23.948
VIrC	3.309	8	0.827	36.538	29.679
VIrGe	8.13	11	1.644	10.757	23.481
VIrSi	7.112	11	1.438	14.245	30.364
VIrSn	9.536	11	1.928	7.459	19.14
VNiAl	1.411	8	0.353	82.188	27.727
VNiB	7.435	3	3.575	3.715	43.682

VNiGa	2.466	11	0.499	50.713	21.417
VNiIn	2.816	3	1.354	9.425	14.656
VOsAs	3.18	3	1.529	12.615	25.884
VOsBi	3.644	3	1.752	8.027	14.302
VOsP	3.072	3	1.477	14.617	32.945
VOsSb	3.483	11	0.704	36.195	21.861
VPtAl	3.013	11	0.609	39.683	19.725
VPtB	6.763	3	3.252	4.216	26.006
VPtGa	4.723	3	2.271	5.58	17.137
VPtTl	4.764	3	2.29	4.403	9.599
VReTe	2.753	11	0.557	49.183	20.366
VRhC	5.386	3	2.589	6.306	41.134
VRhGe	8.75	3	4.206	2.371	26.799
VRhPb	12.27	3	5.899	1.11	12.653
VRhSi	8.628	3	4.148	2.637	38.003
VRhSn	10.81	3	5.197	1.513	20.572
VRuAs	3.868	11	0.782	32.066	31.356
VRuBi	6.888	11	1.393	10.469	15.129
VRuP	3.658	3	1.759	10.506	43.453
VRuSb	5.215	11	1.054	18.175	24.605
VTcTe	2.884	11	0.583	42.645	23.452
WCoAl	1.818	6	0.551	57.275	25.067
WCoB	2.901	8	0.725	51.013	34.205
WCoGa	2.39	6	0.724	39.291	22.46
WCoIn	2.179	6	0.66	38.372	17.223
WFeC	3.373	8	0.843	42.346	34.998
WFeGe	4.867	8	1.217	19.508	26.57
WFeSi	5.317	8	1.329	18.425	34.286
WFeSn	7.217	14	1.242	16.378	21.081
WIrAl	1.382	6	0.419	94.25	24.788
WIrB	2.766	8	0.692	53.712	29.443
WIrGa	1.073	6	0.325	139.898	22.785
WIrIn	1.28	6	0.388	95.602	19.291
WIrTl	1.083	6	0.328	115.43	14.692
WOsGe	2.414	8	0.603	1.115	0.188
WOsPb	3.1	14	0.534	57.688	16.166
WOsSn	3.207	14	0.552	60.673	22.495
WRhAl	1.729	6	0.524	60.648	25.705
WRhB	1.445	8	0.361	132.414	32.079
WRhGa	1.631	6	0.494	67.589	22.988
WRhIn	1.659	6	0.503	58.215	18.786
WRhTl	1.379	6	0.418	72.938	13.97
WRuPb	3.185	14	0.548	51.364	16.132
YAgC	0.755	9	0.174	144.993	9.571
YAgSi	1.227	6	0.372	42.74	10.09
YAuGe	1.168	6	0.354	47.681	6.864
YAuSi	1.318	6	0.399	43.52	8.958
YAuSn	1.213	6	0.367	43.038	6.347
YCoS	10.938	4	4.341	1.445	14.88
YCoTe	8.574	8	2.143	3.684	10.156
YCuC	0.709	8	0.177	170.292	13.348
YCuGe	1.292	6	0.391	40.505	8.906
YCuSi	1.334	6	0.404	41.466	12.422
YHgAl	2.773	6	0.84	10.506	5.878
YHgB	1.524	6	0.462	29.864	6.348
YNiAs	0.974	8	0.243	99.5	11.81
YNiBi	0.837	8	0.209	98.956	5.961

YNiP	1.161	8	0.29	83.496	16.19
YNiSb	0.979	8	0.245	89.458	9.611
YPtAs	0.763	14	0.131	256.551	9.285
YPtBi	0.871	6	0.264	77.731	6.182
YPtP	0.968	8	0.242	108.632	11.022
YPtSb	0.888	6	0.269	84.551	8.753
YRhTe	1.139	8	0.285	76.543	10.473
ZrAgB	2.825	6	0.855	19.278	17.937
ZrAuAl	2.28	6	0.69	24.605	13.318
ZrAuB	2.752	6	0.834	22.486	15.809
ZrAuGa	6.404	6	1.939	5.212	11.294
ZrAuTl	4.329	6	1.311	8.045	7.128
ZrCoAs	6.374	8	1.594	9.034	22.023
ZrCoBi	9.252	8	2.313	4.05	10.823
ZrCoP	8.081	8	2.02	6.976	30.713
ZrCoSb	8.241	8	2.06	5.48	17.458
ZrCuB	2.611	6	0.791	25.041	23.408
ZrFePo	4.951	4	1.965	5.187	11.063
ZrFeS	4.147	4	1.646	8.998	27.06
ZrFeSe	4.882	4	1.938	6.496	20.319
ZrFeTe	4.843	4	1.922	6.157	17.543
ZrIrAs	4.459	8	1.115	15.971	18.216
ZrIrBi	2.838	8	0.71	26.811	11.814
ZrIrP	4.777	8	1.194	15.536	22.455
ZrIrSb	4.72	8	1.18	14.12	17.285
ZrNiC	1.824	8	0.456	69.576	30.211
ZrNiGe	3.453	8	0.863	20.554	19.182
ZrNiPb	2.766	8	0.691	22.874	9.374
ZrNiSi	11.496	8	2.874	3.61	26.606
ZrNiSn	3.499	3	1.682	6.653	14.748
ZrPtPb	2.19	3	1.053	13.438	9.775
ZrPtSi	3.719	6	1.126	15.559	20.274
ZrPtSn	3.084	3	1.483	9.011	14.412
ZrRhAs	2.898	8	0.724	28.884	21.726
ZrRhBi	1.911	8	0.478	44.83	12.261
ZrRhP	4.472	8	1.118	16.286	28.405
ZrRhSb	2.587	8	0.647	31.78	18.575
ZrRuTe	4.87	8	1.218	12.603	19.157

5 Additional Semiconductor Data - Structure.

Table 3: Half-Heusler Structure

Compound	Lattice Parameter (Å)	E_g (eV)	E_g Type	Bulk Modulus (GPa)
AcNiAs	6.583	0.145	PBE	76.206
AcNiP	6.462	0.615	PBE	82.504
AcNiSb	6.826	0.391	PBE	69.803
CoMoAl	5.772	0.306	MBJ	141.056
CrCoAl	5.461	0.545	MBJ	162.610
CrCoB	4.984	0.84	MBJ	239.975
CrCoGa	5.457	0.622	MBJ	168.191
CrCoIn	5.752	0.699	MBJ	139.333
CrFeC	4.895	0.563	MBJ	270.387
CrFeGe	5.450	0.423	MBJ	190.022
CrFeSi	5.339	0.368	MBJ	207.641
CrFeSn	5.743	0.466	MBJ	156.398
CrIrAl	5.760	0.351	MBJ	179.152
CrIrB	5.376	0.528	MBJ	237.306
CrIrGa	5.775	0.361	MBJ	182.999
CrIrIn	6.042	0.476	MBJ	154.748
CrIrTl	6.125	0.584	MBJ	392.268
CrOsGe	5.767	0.354	MBJ	202.465
CrOsPb	6.135	0.338	MBJ	150.077
CrOsSi	5.662	0.31	MBJ	218.221
CrOsSn	6.026	0.419	MBJ	174.263
CrReAs	5.794	0.152	MBJ	197.964
CrReP	5.641	0.123	MBJ	218.949
CrReSb	6.057	0.241	MBJ	174.160
CrRhAl	5.729	0.444	MBJ	159.459
CrRhB	5.315	0.63	MBJ	217.260
CrRhGa	5.733	0.44	MBJ	163.138
CrRuC	5.232	0.36	MBJ	241.483
CrRuGe	5.722	0.203	MBJ	185.993
CrRuPb	6.090	0.333	MBJ	141.803
CrRuSi	5.620	0.147	MBJ	200.581
CrRuSn	5.987	0.287	MBJ	159.508
CrTcAs	5.752	0.162	MBJ	187.237
CrTcP	5.597	0.097	MBJ	206.015
CrTcSb	6.018	0.234	MBJ	162.928
FeMoSi	5.674	0.183	MBJ	176.267
HfAgAl	6.268	0.068	PBE	106.243
HfAgB	5.862	0.147	PBE	135.707
HfAgGa	6.237	0.090	MBJ	107.349
HfAuAl	6.263	0.641	PBE	126.918
HfAuB	5.919	0.72	PBE	152.648
HfAuGa	6.248	0.562	PBE	126.841
HfAuIn	6.461	0.369	PBE	115.610
HfAuTl	6.526	0.254	PBE	107.310
HfCoAs	5.792	1.279	PBE	161.215
HfCoBi	6.186	0.969	PBE	125.393
HfCoP	5.649	1.368	PBE	176.580
HfCoSb	6.054	1.127	PBE	143.683
HfCuB	5.528	0.085	MBJ	156.225
HfFeTe	6.042	0.824	PBE	145.573
HfIrSb	6.320	0.881	PBE	158.922
HfNiC	5.336	0.908	PBE	184.298

HfNiGe	5.849	0.563	PBE	146.182
HfNiSi	5.771	0.685	PBE	157.476
HfNiSn	6.105	0.376	PBE	129.269
HfPdSn	6.343	0.394	PBE	126.208
HfPtGe	6.161	1.138	PBE	154.420
HfPtPb	6.462	0.753	PBE	127.647
HfPtSi	6.082	1.293	PBE	165.434
HfPtSn	6.366	0.906	PBE	143.738
HfRhAs	6.061	0.295	PBE	154.922
HfRhBi	6.404	0.145	PBE	128.435
HfRhP	5.936	0.855	PBE	167.249
HfRhSb	6.282	1.126	PBE	145.615
HfRuTe	6.277	0.066	PBE	147.603
LaAuSi	6.751	0.241	PBE	76.672
LaAuSn	6.995	0.143	PBE	68.537
LaCoS	6.130	0.32	PBE	98.687
LaCoSe	6.295	0.066	PBE	90.744
LaCoTe	6.545	0.632	PBE	83.991
LaCuC	6.009	0.333	PBE	88.674
LaFeF	6.494	0.056	MBJ	35.166
LaHgAl	7.012	0.066	PBE	56.874
LaHgIn	7.165	0.121	PBE	52.197
LaNiAs	6.370	0.626	PBE	86.178
LaNiP	6.247	0.698	PBE	93.785
LaNiSb	6.619	0.453	PBE	78.517
LaPtSb	6.859	0.05	PBE	85.383
LaRhS	6.404	0.366	PBE	96.228
LaRhSe	6.545	0.128	PBE	90.539
LaRhTe	6.760	0.749	PBE	86.242
LaRuF	6.037	0.056	MBJ	82.975
MnNiB	5.057	0.060	PBE	193.676
MoIrB	5.599	0.325	MBJ	242.510
MoIrTl	6.217	0.169	MBJ	165.141
MoOsPb	6.237	0.116	MBJ	173.706
MoRhB	5.529	0.497	MBJ	224.441
NbCoC	5.224	1.446	PBE	237.448
NbCoGe	5.706	1.071	PBE	180.535
NbCoPb	6.051	0.942	PBE	141.093
NbCoSi	5.623	0.862	PBE	193.214
NbCoSn	5.962	0.982	PBE	156.446
NbFeAs	5.694	0.581	PBE	188.598
NbFeBi	6.081	0.596	PBE	145.740
NbFeP	5.552	0.507	PBE	209.284
NbFeSb	5.951	0.507	PBE	166.863
NbIrC	5.656	0.283	PBE	216.764
NbIrGe	6.019	0.634	PBE	191.362
NbIrPb	6.321	0.715	PBE	157.385
NbIrSi	5.941	0.485	PBE	204.370
NbIrSn	6.230	0.631	PBE	174.466
NbNiAl	5.771	0	PBE	149.911
NbNiB	5.349	0.58	PBE	207.562
NbNiTl	6.045	0.091	PBE	130.811
NbOsAs	6.015	0.242	PBE	195.936
NbOsBi	6.346	0.318	PBE	162.956
NbOsP	5.893	0.16	PBE	212.157
NbOsSb	6.226	0.264	PBE	183.893
NbPtAl	6.065	0.143	PBE	165.732

NbPtB	5.741	0.808	PBE	203.722
NbPtGa	6.058	0.457	PBE	168.077
NbPtIn	6.274	0.449	PBE	150.271
NbPtTl	6.337	0.592	PBE	142.360
NbRhC	5.567	1.048	PBE	212.120
NbRhGe	5.972	0.649	PBE	176.010
NbRhPb	6.279	0.763	PBE	142.467
NbRhSi	5.896	0.473	PBE	187.189
NbRhSn	6.193	0.659	PBE	158.157
NbRuAs	5.962	0.332	PBE	185.055
NbRuBi	6.303	0.421	PBE	151.150
NbRuP	5.839	0.245	PBE	200.906
NbRuSb	6.184	0.356	PBE	170.766
ScAgC	5.736	0.228	PBE	106.520
ScAuGe	6.268	0.297	PBE	98.743
ScAuSi	6.174	0.386	PBE	109.741
ScAuSn	6.493	0.146	PBE	92.178
ScCdIn	6.676	0.068	MBJ	58.410
ScCdTl	6.748	0.113	MBJ	52.036
ScCoS	5.585	0.672	PBE	132.323
ScCoSe	5.776	0.292	PBE	121.174
ScCoTe	6.043	0.889	PBE	113.128
ScCuC	5.352	0.118	PBE	131.888
ScHgAl	6.441	0.103	PBE	76.804
ScHgB	6.029	0.17	PBE	94.817
ScHgGa	6.431	0.077	PBE	73.059
ScHgIn	6.665	0.378	MBJ	67.349
ScHgTl	6.760	0.153	MBJ	57.973
ScNiAs	5.822	0.467	PBE	119.007
ScNiBi	6.247	0.179	PBE	90.751
ScNiP	5.669	0.58	PBE	132.603
ScNiSb	6.103	0.263	PBE	105.623
ScPtP	6.019	0.085	PBE	131.587
ScPtSb	6.375	0.659	PBE	116.107
ScRhTe	6.294	0.463	PBE	113.466
TaCoC	5.216	1.536	PBE	239.881
TaCoGe	5.698	1.206	PBE	191.789
TaCoPb	6.041	0.973	PBE	149.931
TaCoSi	5.614	1.238	PBE	205.737
TaCoSn	5.952	1.039	PBE	166.828
TaFeAs	5.688	0.9205	PBE	198.364
TaFeBi	6.072	0.92	PBE	154.273
TaFeP	5.545	0.837	PBE	220.237
TaFeSb	5.943	0.856	PBE	177.775
TaIrGe	6.013	0.932	PBE	202.793
TaIrSi	5.935	0.795	PBE	215.602
TaIrSn	6.219	0.942	PBE	185.752
TaNiAl	5.760	0.585	MBJ	161.643
TaNiB	5.338	0.778	PBE	217.954
TaNiGa	5.737	0.243	PBE	168.074
TaNiIn	5.989	0.181	PBE	145.008
TaNiTl	6.032	0.427	MBJ	138.713
TaOsBi	6.338	0.132	MBJ	170.245
TaOsP	5.890	0.049	PBE	219.375
TaOsSb	6.217	0.551	PBE	193.959
TaPtAl	6.052	0.572	PBE	178.819
TaPtB	5.733	1.327	PBE	215.282

TaPtGa	6.045	0.94	PBE	181.458
TaPtIn	6.259	0.923	PBE	161.870
TaPtTl	6.322	0.952	PBE	152.878
TaRhC	5.557	0.645	PBE	214.239
TaRhGe	5.961	1.07	PBE	186.818
TaRhPb	6.266	1.049	PBE	151.718
TaRhSi	5.885	0.868	PBE	197.920
TaRhSn	6.180	1.047	PBE	168.556
TaRuAs	5.955	0.452	PBE	193.138
TaRuBi	6.293	0.455	PBE	159.409
TaRuP	5.831	0.533	PBE	208.181
TaRuSb	6.175	0.631	PBE	180.683
TiAgAl	6.112	0.151	PBE	98.093
TiAgB	5.660	0.337	PBE	133.312
TiAgGa	6.088	0.177	PBE	98.730
TiAgIn	6.342	0.072	PBE	86.833
TiAuAl	6.094	0.695	PBE	120.029
TiAuB	5.700	0.864	PBE	154.407
TiAuGa	6.090	0.622	PBE	119.601
TiAuIn	6.337	0.424	PBE	105.515
TiAuTl	6.419	0.326	PBE	96.077
TiCoAs	5.601	1.3	PBE	164.368
TiCoBi	6.026	0.896	PBE	123.841
TiCoP	5.440	1.375	PBE	185.328
TiCoSb	5.881	1.053	PBE	143.102
TiCuB	5.300	0.216	PBE	159.657
TiCuGa	5.773	0.065	PBE	113.889
TiFePo	6.035	0.69	PBE	125.729
TiFeS	5.412	1.101	PBE	177.363
TiFeSe	5.604	0.901	PBE	159.409
TiFeTe	5.874	0.957	PBE	146.945
TiIrAs	5.931	0.758	PBE	170.904
TiIrBi	6.302	0.617	PBE	138.221
TiIrP	5.791	0.896	PBE	188.372
TiIrSb	6.165	0.807	PBE	159.534
TiNiC	5.099	0.97	PBE	203.885
TiNiGe	5.661	0.625	PBE	146.947
TiNiPb	6.042	0.339	PBE	110.792
TiNiSi	5.568	0.743	PBE	159.361
TiNiSn	5.942	0.442	PBE	125.264
TiOsTe	6.163	0.478	PBE	161.820
TiPtC	5.553	0.418	PBE	181.595
TiPtGe	5.983	0.845	PBE	154.395
TiPtPb	6.330	0.712	PBE	121.255
TiPtSi	5.889	0.863	PBE	167.809
TiPtSn	6.218	0.764	PBE	139.058
TiRhAs	5.882	0.795	PBE	157.132
TiRhBi	6.264	0.69	PBE	124.931
TiRhP	5.740	0.799	PBE	173.820
TiRhSb	6.130	0.719	PBE	143.445
TiRuTe	6.126	0.745	PBE	148.165
VCoC	4.948	0.936	PBE	251.033
VCoGe	5.507	0.66	PBE	177.083
VCoPb	5.899	0.638	PBE	130.946
VCoSi	5.404	0.526	PBE	193.569
VCoSn	5.795	0.614	PBE	149.172
VFeAs	5.491	0.342	PBE	189.975

VFeBi	5.927	0.332	PBE	138.494
VFeP	5.325	0.302	PBE	214.973
VFeSb	5.782	0.321	PBE	162.745
VIrC	5.386	0.305	PBE	229.091
VIrGe	5.831	0.295	PBE	188.927
VIrSi	5.732	0.184	PBE	204.679
VIrSn	6.080	0.293	PBE	166.402
VNiAl	5.578	0.12	PBE	143.521
VNiB	5.088	0.904	PBE	209.252
VNiGa	5.560	0.319	PBE	148.818
VNiIn	5.847	0.223	PBE	123.720
VOsAs	5.822	0.079	PBE	198.697
VOsBi	6.208	0.119	PBE	155.111
VOsP	5.674	1.099	MBJ	218.599
VOsSb	6.070	0.109	PBE	178.244
VPtAl	5.876	1.015	MBJ	157.257
VPtB	5.488	0.369	PBE	205.983
VPtGa	5.881	0.167	PBE	159.105
VPtTl	6.222	0.29	PBE	127.158
VReTe	6.107	0.244	MBJ	170.237
VRhC	5.301	0.452	PBE	218.964
VRhGe	5.787	0.319	PBE	170.445
VRhPb	6.147	0.405	PBE	132.571
VRhSi	5.690	0.187	PBE	185.625
VRhSn	6.042	0.346	PBE	149.417
VRuAs	5.773	0.14	PBE	184.823
VRuBi	6.166	0.199	PBE	143.372
VRuP	5.625	0.074	PBE	204.176
VRuSb	6.029	0.176	PBE	163.953
VTcTe	6.074	0.727	MBJ	158.193
WCoAl	5.630	0.455	MBJ	195.013
WCoB	5.232	0.753	PBE	262.595
WCoGa	5.622	0.346	PBE	201.667
WCoIn	5.874	0.377	PBE	171.453
WFeC	5.164	0.518	PBE	273.211
WFeGe	5.623	0.201	PBE	218.169
WFeSi	5.532	0.048	PBE	235.323
WFeSn	5.875	0.235	PBE	188.992
WIrAl	5.929	0.143	MBJ	212.737
WIrB	5.627	0.591	MBJ	257.422
WIrGa	5.933	0.233	MBJ	215.895
WIrIn	6.149	0.363	MBJ	192.332
WIrTl	6.214	0.577	MBJ	180.593
WOsGe	5.937	0.104	MBJ	4.356
WOsPb	6.238	0.347	MBJ	187.378
WOsSn	6.147	0.244	MBJ	207.395
WRhAl	5.889	0.206	MBJ	191.566
WRhB	5.553	0.764	MBJ	239.525
WRhGa	5.884	0.266	MBJ	195.501
WRhIn	6.107	0.23	MBJ	172.840
WRhTl	6.163	0.078	PBE	163.997
WRuPb	6.192	0.159	MBJ	173.822
YAgC	6.061	0.851	MBJ	88.025
YAgSi	6.450	0.113	MBJ	80.654
YAuGe	6.539	0.324	MBJ	83.594
YAuSi	6.458	0.239	PBE	91.420
YAuSn	6.736	0.077	MBJ	79.890

YCoS	5.874	0.061	PBE	108.870
YCoTe	6.296	0.872	PBE	96.335
YCuC	5.698	0.085	PBE	105.963
YCuGe	6.233	0.299	MBJ	82.585
YCuSi	6.158	0.559	MBJ	88.692
YHgAl	6.715	0.084	PBE	67.389
YHgB	6.355	0.096	PBE	78.041
YNiAs	6.101	0.492	PBE	99.593
YNiBi	6.493	0.193	PBE	78.934
YNiP	5.964	0.594	PBE	108.756
YNiSb	6.359	0.285	PBE	90.264
YPtAs	6.423	0.826	MBJ	101.692
YPtBi	6.746	0.424	MBJ	87.827
YPtP	6.305	0.917	MBJ	107.722
YPtSb	6.615	0.094	PBE	98.290
YRhTe	6.530	0.158	PBE	96.961
ZrAgB	5.925	0.24	PBE	127.111
ZrAuAl	6.316	0.472	PBE	117.633
ZrAuB	5.976	0.79	PBE	142.609
ZrAuGa	6.300	0.594	PBE	117.321
ZrAuTl	6.572	0.344	PBE	100.641
ZrCoAs	5.836	1.208	PBE	151.444
ZrCoBi	6.223	0.985	PBE	118.732
ZrCoP	5.699	1.284	PBE	166.917
ZrCoSb	6.094	1.057	PBE	135.048
ZrCuB	5.587	0.084	PBE	146.730
ZrFePo	6.232	0.096	PBE	119.041
ZrFeS	5.669	0.326	PBE	158.293
ZrFeSe	5.838	0.112	PBE	145.997
ZrFeTe	6.084	1.156	PBE	136.714
ZrIrAs	6.157	0.265	PBE	156.638
ZrIrBi	6.480	0.204	PBE	133.524
ZrIrP	6.038	0.782	PBE	168.954
ZrIrSb	6.358	1.407	PBE	150.824
ZrNiC	5.397	0.953	PBE	178.536
ZrNiGe	5.895	0.665	PBE	137.365
ZrNiPb	6.239	0.365	PBE	109.603
ZrNiSi	5.818	0.786	PBE	146.561
ZrNiSn	6.148	0.486	PBE	120.938
ZrPtPb	6.502	0.826	PBE	120.947
ZrPtSi	6.129	1.337	PBE	155.002
ZrPtSn	6.407	0.974	PBE	135.589
ZrRhAs	6.104	1.204	PBE	148.399
ZrRhBi	6.443	1.023	PBE	123.348
ZrRhP	5.984	1.427	PBE	160.409
ZrRhSb	6.324	1.18	PBE	137.754
ZrRuTe	6.318	0.888	PBE	141.107

6 Additional Semiconductor Data - TE Quality Factor, β .

Table 4: β Predictions

Compound	β_n	β_p
AcNiAs	34.134	16.016
AcNiP	3.49	6.702
AcNiSb	4.487	47.799
CoMoAl	10.671	28.335
CrCoAl	1.517	13.314
CrCoB	3.046	5.148
CrCoGa	2.742	18.875
CrCoIn	3.845	20.981
CrFeC	1.546	3.986
CrFeGe	2.086	3.349
CrFeSi	1.012	2.971
CrFeSn	3.528	9.109
CrIrAl	1.955	14.202
CrIrB	1.72	7.971
CrIrGa	2.805	16.603
CrIrIn	2.237	19.349
CrIrTl	1.305	82.541
CrOsGe	1.71	6.763
CrOsPb	2.82	21.259
CrOsSi	1.123	5.717
CrOsSn	1.852	16.21
CrReAs	1.724	6.355
CrReP	1.738	5.752
CrReSb	1.557	7.904
CrRhAl	1.158	8.416
CrRhB	1.953	7.91
CrRhGa	1.582	13.879
CrRuC	1.196	5.224
CrRuGe	1.542	12.278
CrRuPb	2.466	21.667
CrRuSi	0.915	10.169
CrRuSn	1.709	15.217
CrTcAs	1.47	30.813
CrTcP	0.966	29.387
CrTcSb	1.781	30.895
FeMoSi	0.965	5.206
HfAgAl	6.512	1.927
HfAgB	5.447	3.693
HfAgGa	7.068	3.059
HfAuAl	5.684	1.722
HfAuB	5.046	3.998
HfAuGa	6.223	3.011
HfAuIn	6.915	3.575
HfAuTl	8.999	23.766
HfCoAs	2.282	6.018
HfCoBi	3.597	15.348
HfCoP	2.097	5.241
HfCoSb	2.883	5.871
HfCuB	5.855	3.205
HfFeTe	6.95	8.022
HfIrSb	12.742	3.071

HfNiC	3.085	4.478
HfNiGe	3.997	3.095
HfNiSi	3.368	1.91
HfNiSn	4.631	3.328
HfPdSn	4.739	3.727
HfPtGe	3.586	3.823
HfPtPb	5.503	5.3
HfPtSi	3.276	2.728
HfPtSn	4.351	3.744
HfRhAs	11.844	3.715
HfRhBi	16.492	4.874
HfRhP	6.18	3.159
HfRhSb	2.641	3.411
HfRuTe	64.32	2.082
LaAuSi	14.3	15.856
LaAuSn	17.556	54.069
LaCoS	30.347	6.495
LaCoSe	60.886	7.472
LaCoTe	11.238	0.337
LaCuC	3.789	5.661
LaFeF	8.288	3.911
LaHgAl	32.005	34.815
LaHgIn	8.808	28.036
LaNiAs	13.558	0.352
LaNiP	10.904	7.004
LaNiSb	16.116	0.944
LaPtSb	179.94	53.926
LaRhS	59.1	3.811
LaRhSe	79.688	1.308
LaRhTe	14.972	1.615
LaRuF	16.932	0.426
MnNiB	0.527	1.312
MoIrB	3.022	9.412
MoIrTl	4.446	36.728
MoOsPb	3.096	22.26
MoRhB	2.804	22.408
NbCoC	1.095	4.41
NbCoGe	4.262	9.4
NbCoPb	2.888	14.765
NbCoSi	1.843	2.251
NbCoSn	9.071	9.427
NbFeAs	4.106	5.439
NbFeBi	5.137	8.875
NbFeP	3.433	4.521
NbFeSb	4.027	8.278
NbIrC	10.311	9.04
NbIrGe	7.908	48.052
NbIrPb	6.29	18.779
NbIrSi	4.971	12.71
NbIrSn	5.326	16.052
NbNiAl	5.327	21.862
NbNiB	1.866	4.135
NbNiTl	3.598	33.139
NbOsAs	5.101	10.711
NbOsBi	5.996	12.736
NbOsP	5.283	9.259
NbOsSb	5.383	9.805

NbPtAl	6.471	7.191
NbPtB	5.039	6.439
NbPtGa	7.769	7.52
NbPtIn	6.768	10.626
NbPtTl	2.551	33.771
NbRhC	1.848	5.55
NbRhGe	4.469	5.01
NbRhPb	4.825	4.759
NbRhSi	3.655	4.843
NbRhSn	4.132	3.578
NbRuAs	4.342	7.514
NbRuBi	5.163	9.968
NbRuP	3.667	6.237
NbRuSb	4.301	7.572
ScAgC	2.539	4.394
ScAuGe	4.262	4.681
ScAuSi	3.498	3.535
ScAuSn	4.864	4.599
ScCdIn	4.052	3.532
ScCdTl	5.783	12.857
ScCoS	3.123	0.649
ScCoSe	6.92	1.608
ScCoTe	1.946	2.258
ScCuC	2.369	3.634
ScHgAl	5.372	2.707
ScHgB	4.608	4.331
ScHgGa	6.111	3.933
ScHgIn	6.541	4.258
ScHgTl	8.541	15.121
ScNiAs	2.143	3.132
ScNiBi	4.086	5.735
ScNiP	1.473	2.141
ScNiSb	2.781	3.45
ScPtP	16.906	2.543
ScPtSb	2.902	4.875
ScRhTe	4.505	4.046
TaCoC	1.837	7.18
TaCoGe	2.462	12.374
TaCoPb	3.673	21.24
TaCoSi	1.965	4.47
TaCoSn	2.86	12.222
TaFeAs	5.364	8.05
TaFeBi	3.059	10.481
TaFeP	5.009	6.933
TaFeSb	22.982	7.791
TaIrGe	6.547	8.485
TaIrSi	6.176	6.271
TaIrSn	28.408	7.052
TaNiAl	3.92	40.677
TaNiB	3.329	12.304
TaNiGa	4.198	40.332
TaNiIn	4.54	29.256
TaNiTl	6.084	24.585
TaOsBi	3.89	14.93
TaOsP	13.24	11.253
TaOsSb	6.346	11.861
TaPtAl	6.776	11.162

TaPtB	5.153	1.716
TaPtGa	6.208	14.719
TaPtIn	3.712	2.659
TaPtTl	3.532	28.83
TaRhC	9.259	10.749
TaRhGe	5.133	7.614
TaRhPb	3.482	2.148
TaRhSi	5.234	4.751
TaRhSn	4.147	8.237
TaRuAs	7.243	9.601
TaRuBi	11.097	12.121
TaRuP	5.183	8.502
TaRuSb	5.546	9.217
TiAgAl	3.2	1.071
TiAgB	2.272	1.637
TiAgGa	3.646	1.549
TiAgIn	3.749	1.873
TiAuAl	2.457	1.098
TiAuB	2.2	2.11
TiAuGa	2.908	1.643
TiAuIn	3.323	1.947
TiAuTl	4.428	19.956
TiCoAs	1.147	0.867
TiCoBi	2.143	1.749
TiCoP	0.911	3.807
TiCoSb	1.461	5.982
TiCuB	2.313	1.271
TiCuGa	4.062	1.382
TiFePo	5.941	10.215
TiFeS	1.886	3.248
TiFeSe	3.116	4.737
TiFeTe	2.652	4.983
TiIrAs	21.5	1.809
TiIrBi	3.467	2.543
TiIrP	3.274	1.514
TiIrSb	2.381	1.816
TiNiC	1.216	1.467
TiNiGe	1.989	1.318
TiNiPb	3.427	2.914
TiNiSi	1.477	0.74
TiNiSn	2.376	1.632
TiOsTe	10.355	1.549
TiPtC	11.588	1.591
TiPtGe	2.045	1.975
TiPtPb	1.997	3.067
TiPtSi	3.115	1.375
TiPtSn	1.608	1.943
TiRhAs	2.447	1.489
TiRhBi	1.73	2.362
TiRhP	2.125	1.348
TiRhSb	1.609	1.573
TiRuTe	2.084	1.356
VCoC	2.214	5.6
VCoGe	2.342	3.095
VCoPb	2.271	1.433
VCoSi	2.089	2.497
VCoSn	1.936	5.354

VFeAs	2.529	4.6
VFeBi	2.246	6.85
VFeP	2.261	26.847
VFeSb	12.835	4.912
VIrC	2.558	8.303
VIrGe	3.892	7.882
VIrSi	3.778	7.156
VIrSn	3.739	7.74
VNiAl	0.984	9.285
VNiB	1.073	0.803
VNiGa	1.552	13.924
VNiIn	1.351	2.534
VOsAs	3.827	2.142
VOsBi	2.719	2.789
VOsP	3.742	1.89
VOsSb	3.214	13.283
VPtAl	4.116	14.168
VPtB	3.925	1.405
VPtGa	3.603	2.043
VPtTl	1.798	23.346
VReTe	3.157	15.68
VRhC	2.589	1.083
VRhGe	7.775	0.967
VRhPb	1.718	21.472
VRhSi	2.532	0.749
VRhSn	2.601	0.973
VRuAs	2.817	9.017
VRuBi	2.418	10.255
VRuP	2.572	1.206
VRuSb	2.94	8.521
VTcTe	3.328	34.722
WCoAl	6.005	8.013
WCoB	7.271	8.936
WCoGa	7.152	7.848
WCoIn	15.265	9.197
WFeC	6.635	8.302
WFeGe	7.75	7.008
WFeSi	7.933	5.555
WFeSn	6.794	13.223
WIrAl	3.93	10.419
WIrB	9.303	10.472
WIrGa	5.121	13.393
WIrIn	8.232	12.674
WIrTl	7.743	41.701
WOsGe	9.744	30.129
WOsPb	8.976	28.385
WOsSn	4.15	22.122
WRhAl	2.964	7.91
WRhB	8.955	13.206
WRhGa	6.186	9.35
WRhIn	6.044	10.01
WRhTl	6.856	36.704
WRuPb	8.362	25.959
YAgC	5.616	28.319
YAgSi	3.879	10.425
YAuGe	23.151	16.358
YAuSi	11.682	12.752

YAuSn	17.698	16.524
YCoS	8.372	1.456
YCoTe	2.242	5.763
YCuC	3.62	21.515
YCuGe	4.372	11.725
YCuSi	3.626	16.372
YHgAl	17.707	9.166
YHgB	5.676	14.075
YNiAs	2.668	18.898
YNiBi	4.834	32.497
YNiP	2.136	13.548
YNiSb	3.36	20.98
YPtAs	7.829	33.973
YPtBi	9.258	22.748
YPtP	12.982	21.985
YPtSb	32.755	24.938
YRhTe	10.029	18.882
ZrAgB	9.681	5.603
ZrAuAl	11.602	7.943
ZrAuB	9.576	7.244
ZrAuGa	12.723	5.027
ZrAuTl	6.378	27.894
ZrCoAs	1.678	4.991
ZrCoBi	2.938	6.367
ZrCoP	1.267	3.422
ZrCoSb	2.073	4.813
ZrCuB	10.434	5.196
ZrFePo	11.588	3.444
ZrFeS	5.156	2.082
ZrFeSe	8.054	2.319
ZrFeTe	1.326	2.528
ZrIrAs	17.353	7.734
ZrIrBi	61.934	13.331
ZrIrP	52.883	6.494
ZrIrSb	5.158	7.585
ZrNiC	1.85	9.088
ZrNiGe	2.836	7.509
ZrNiPb	22.131	14.006
ZrNiSi	2.066	2.807
ZrNiSn	3.24	2.161
ZrPtPb	4.507	4.319
ZrPtSi	6.161	5.125
ZrPtSn	3.407	2.674
ZrRhAs	1.863	7.957
ZrRhBi	6.412	15.044
ZrRhP	3.404	5.071
ZrRhSb	1.886	9.247
ZrRuTe	4.98	6.284
